Weak Coherent Pulse Source and Polarization Control for Quantum Key Distribution

by

Wilson Wu

A thesis
presented to the University of Waterloo
in fulfillment of the
thesis requirement for the degree of
Master of Science
in
Physics (Quantum Information)

Waterloo, Ontario, Canada, 2023

Author's Declaration

This thesis consists of material all of which I authored or co-authored: see Statement of Contributions included in the thesis. This is a true copy of the thesis, including any required final revisions, as accepted by my examiners.

I understand that my thesis may be made electronically available to the public.

Statement of Contributions

This thesis contains work completed in collaboration with others where I have made the major contribution. The contributions are listed below:

Chapters 0 and 1

Wilson Wu wrote the introductory chapters.

Chapter 2

Wilson Wu wrote the wave packet model simulation.

Wilson Wu, Ramy Tannous, and Paul Godin measured the pulsed laser source spectrum.

Wilson Wu and Paul Godin build the fiber connectorization and alignment system and spliced fibers for the weak coherent pulse source.

Chapter 3

Wilson Wu measured the temperature sensitivity and polarization stability of polarization maintaining (PM) fiber.

Wilson Wu and Ramy Tannous measured the PM fiber phase sensitivity to dynamic motion.

Chapter 4

Wilson Wu measured the polarization sensitivity of PM fiber of a fiber squeezer.

Wilson Wu and Kimia Mohammadi built the set up and measured the polarization sensitivity of PM fiber in a motorized paddle controller.

Wilson Wu, Kimia Mohammadi, Paul Godin, and Ramy Tannous were involved in designing and testing the v-groove solution. The v-grooves were machined by the University of Waterloo science machine shop.

Wilson Wu and Ramy Tannous built the set up and characterized the optical components for free-space polarization control.

Diagrams were generated in InkScape with the use of graphical components from the ComponentLibrary by Alexander Franzen, under the CC BY-NC 3.0 license.

Abstract

The Quantum EncrYption and Science Satellite will demonstrate quantum communication from space. One demonstration will be a satellite uplink using a weak coherent pulse source. This thesis will discuss work in minimizing the quantum bit error rate of polarization-encoded states produced by the weak coherent pulse source, including a wave packet model developed to quantify fiber length and angular alignment tolerances within the system. In addition, the weak coherent pulse sources makes use of polarization-maintaining fibers, requiring a polarization control system to compensate for phase shifts induced in the fiber during operation of the quantum uplink. Methods for polarization control in polarization-maintaining fiber are explored and compared.

Acknowledgements

Table of Contents

List of Figures

List of Abbreviations

APT acquisition, pointing, and tracking.

AWG arbitrary waveform generator.

BS beam splitter.

CSA Canadian Space Agency.

CW continuous-wave.

DGD differential group delay.

EPS entangled-pair source.

HWP half-wave plate.

LCR liquid crystal retarder.

LP linear polarization.

MZI Mach-Zehnder interferometer.

NIST National Institute of Standards and Technology.

PANDA Polarization-Maintaining And Absorption-Reducing.

PBS polarizing beam splitter.

PLOB Pirandola-Laurenza-Ottaviani-Banchi.

PM polarization-maintaining.

PMod phase modulator.

PPLN periodically poled lithium niobate.

PQC post-quantum cryptography.

QBER quantum bit error rate.

QEYSSat Quantum EncrYption and Science Satellite.

QKD quantum key distribution.

QOGS Quantum Optical Ground Station.

QRNG quantum random number generator.

QWP quarter-wave plate.

RAC Research Advancement Center.

SFG sum-frequency generation.

SM single mode.

TEC thermoelectric cooler.

WCPS weak coherent pulse source.

WDM wavelength division multiplexer.

Chapter 1

Introduction

Quantum key distribution (QKD) is a technology that can provide provably secure communication. Ground-based QKD systems are already commercially available today, although such links are limited in transmission distance by losses in fiber. Satellite links can enable quantum communication over greater distances.

The Quantum EncrYption and Science Satellite (QEYSSat) mission will demonstrate QKD in a ground-to-satellite link. One of the photon sources to be used in an uplink demonstration is a WCPS to implement the decoy-state BB84 protocol. The source uses polarization-maintaining (PM) fiber links throughout the system. Such fiber links will be exposed to outdoor temperatures and various mechanical stresses at the transceiver telescope of the Quantum Optical Ground Station (QOGS) during typical operation, inducing a phase shift on quantum signals transmitted through the PM fiber.

Such phase shifts must be actively monitored and corrected in real time, since they alter the polarization states used in the protocol. In this thesis, various options for polarization control are explored, in order to design and construct a polarization control system for the WCPS.

The first chapter is an overview of quantum key distribution (QKD) in free-space. The background quantum information and optics theory needed for the weak coherent pulse source is discussed. The decoy state BB84 protocol, which will be demonstrated with the weak coherent pulse source, is also introduced.

The second chapter describes the weak coherent pulse source (WCPS), focusing

on the fiber-based phase modulation scheme. A model was developed to estimate the tolerances on the fiber-based system in order to reach a given target QBER. Details on characterization of the WCPS are presented with a discussion on future improvements.

The third chapter discusses polarization-maintaining (PM) fibers, used throughout the WCPS and the link to the quantum optical ground station (QOGS). Their phase sensitivity to the different environmental factors expected during ground station operation is characterized and a total combined phase drift is estimated.

The fourth chapter investigates various methods of polarization control in free-space and within PM fiber. The results are summarized to compare the different advantages and drawbacks of each method. A scheme for the full polarization control loop is described.

The fifth chapter concludes the thesis and describes future work.

Chapter 2

Free-space quantum key distribution

2.1 Quantum key distribution

Quantum key distribution (QKD) enables secure communication through the exchange of secret keys between two distant parties. In contrast with prevalent forms of modern day cryptographic schemes, the security of QKD is granted by the laws of physics rather than an assumption of computational hardness [Sca+09]. This assumption has been challenged by the development of Shor's algorithm, which can be used to break public-key cryptography schemes such as the widely used Rivest-Shamir-Adleman (RSA) scheme [Pir+20].

Although a fault-tolerant quantum computer capable of implementing Shor's algorithm does not yet exist, the continued effort to build quantum computers has sparked a search for quantum-resistant communication methods. One possibility is post-quantum cryptography (PQC), which rely on algorithms believed to be resistant to cryptanalytic attack from both classical and quantum computers [BL17]. Candidate PQC algorithms are currently in the process of standardization by National Institute of Standards and Technology (NIST) [Ala+19].

QKD is a different secure communication technology, whose security proofs additionally allow the quantification of the security of QKD systems. Commercial solutions for fiber-based implementations already exist [Sca+09]. However, fiber-

based implementations are limited by a range of hundreds of kilometers due to losses which scale exponentially at $\sim 0.2 \mathrm{dB\,km^{-1}}$ for commercial fibers [Yan+12], limiting fiber-based quantum communication to inter-city networks [Aws+22]. To enable quantum communication across and between continents with existing technology, satellite links are necessary. Losses scale quadratically in free space [And06], allowing transmission over much longer distances in free-space provided a direct line of sight.

2.2 Photons and polarization

2.2.1 Quantum harmonic oscillator

In classical physics, light is described by Maxwell's equations. However, a quantum mechanical description of light is needed to describe physical systems such as those involving light intensities near the single photon level. This allows light to be quantized, leading to the concept of a photon [KL10].

The modes of the electromagnetic field correspond to quantum harmonic oscillators of different energies. For a given quantum harmonic oscillator, the corresponding Hamiltonian is given by

$$\hat{H} = \frac{1}{2}(\hat{p}^2 + \omega^2 \hat{q}^2), \tag{2.2.1}$$

with commutation relation $[\hat{q}, \hat{p}] = i\hbar$ [Bv05].

The non-Hermitian creation and annihilation operators $\hat{a}$ and $\hat{a}^\dagger$ can be written in terms of $\hat{q}$ and $\hat{p}$ as

$$\hat{a} = \frac{1}{\sqrt{2\hbar\omega}}(\omega\hat{q} + i\hat{p}) \tag{2.2.2}$$

$$\hat{a}^\dagger = \frac{1}{\sqrt{2\hbar\omega}}(\omega\hat{q} - i\hat{p}), \tag{2.2.3}$$

with commutation relation $[\hat{a}, \hat{a}^\dagger] = 1$, allowing the Hamiltonian to be rewritten as [GK04]

$$\hat{H} = \hbar\omega(\hat{a}^\dagger\hat{a} + \frac{1}{2}). \tag{2.2.4}$$

The product $\hat{a}^\dagger\hat{a}$ is the number operator $\hat{n} := \hat{a}^\dagger\hat{a}$ and has a discrete spectrum of

eigenvalues $n = 0, 1, 2, 3, \ldots$ for the eigenvalue equation

$$\hat{n} \ket{n} = n \ket{n}. \tag{2.2.5}$$

The states $\ket{n}$, labeled by their eigenvalues, are known as the Fock states. The set of Fock states $\{\ket{n_k}\}$ for integers $\{n_k\}$ form a complete orthonormal basis for the Fock space [Gla06].

2.2.2 Coherent state

One important quantum optical state is the coherent state, which is a good approximation of laser output for single-mode lasers, provided the laser is operated far above threshold [Lou00]. Additionally, coherent states are eigenvectors of the annihilation operator, satisfying

$$\hat{a} \ket{\alpha} = \alpha \ket{\alpha} \tag{2.2.6}$$

for $\alpha = |\alpha| e^{i\theta}$.

A recursion relation of the coherent state photon number distribution is obtained by taking the inner product of (2.2.6) with Fock state $\ket{n}$,

$$\sqrt{n+1} \braket{n+1|\alpha} = \alpha \braket{n|\alpha}, \tag{2.2.7}$$

leading to the coherent state expansion in the Fock basis

$$\ket{\alpha} = e^{-\frac{|\alpha|^2}{2}} \sum_{n=0}^{\infty} \frac{\alpha^n}{\sqrt{n!}} \ket{n}. \tag{2.2.8}$$

The photon number distribution $P(n)$ of the coherent state can be obtained from the inner product

$$P(n) = |\braket{n|\alpha}|^2 = \frac{|\alpha|^{2n}}{n!} e^{-|\alpha|^2}. \tag{2.2.9}$$

Coherent states display Poissonian photon statistics, with a mean photon number of $|\alpha|^2$ [Gla06].

Weak coherent pulses are formed by attenuation of a laser pulse. For quantum

key distribution (QKD) using weak coherent states, the average photon number is typically much smaller than 1. Weak coherent pulses are commonly used as a photon source for QKD due to their relative ease of implementation, requiring only a pulsed laser source, driving electronics, and appropriate attenuators. Due to the low intensities, many pulses do not contain any photons. Moreover, key rates may be improved by using higher repetition rates – gigahertz rate sources for QKD have been demonstrated [Grü+20]. Nevertheless, the transmission is still limited over high loss channels due to dark counts from detectors, as the signal-to-noise ratio between genuine photon detections and dark counts become too low to produce key [Gis+02].

An additional consideration is the phase of the coherent pulses, which is generally assumed to be completely random. In this scenario, the phase randomized coherent pulses can be written as [ILM07]

$$\rho_{coherent} = \frac{1}{2\pi} \int_0^{2\pi} \left| |\alpha| e^{i\phi} \right\rangle \left\langle |\alpha| e^{i\phi} \right| \mathrm{d}\phi \qquad (2.2.10)$$

$$= \sum_{k=0}^{\infty} e^{-|\alpha|^2} \frac{|\alpha|^{2k}}{k} \left\langle k | k \right\rangle \qquad (2.2.11)$$

Although this assumption is used in security proofs of decoy-state QKD, it does not necessarily hold in practical implementations, particularly high-performance implementations where pulses are generated at repetition rates in the gigahertz regime [KTO14], and subsequent pulses may contain phase correlations. For example, gain-switched laser sources may have residual photons from a previous lasing interval that can seed a suceeding laser pulse, introducing phase correlations. These correlations have been measured [Grü+20; KTO14] and should be characterized in a QKD system in order to evaluate the security of a practical implementation of a gigahertz laser source. Moreover, QKD is still possible with weak coherent pulses of nonrandom phases, albeit with lower key rates. Such an implementation will also fail to produce positive key at lower levels of loss compared with QKD with a phase randomized source [LP07].

2.2.3 Polarization

Quantum information can be encoded along the various degrees of freedom of a photon, such as spatial modes, temporal modes, frequency, and orbital angular momentum (OAM) [KL10]. A commonly used degree of freedom is polarization.

The electric field of monochromatic light travelling in a plane wave along the $\hat{z}$ axis can be described as

$$\mathbf{E}_x = A_x \cos(kz - \omega t)\hat{x}$$
$$\mathbf{E}_y = A_y \cos(kz - \omega t + \phi)\hat{y}. \qquad (2.2.12)$$

for components $\mathbf{E}_x$ and $\mathbf{E}_y$ where the E-field is vibrating along $\hat{x}$ and $\hat{y}$. The polarization state of the light is given by the ratio A_x/A_y between the amplitudes and the relative phase ϕ between the linear components [Hec17].

The polarization state can be visualized on the Poincaré sphere, where each polarization state corresponds to a point on the Poincaré sphere [Iiz02]. A Poincaré sphere is depicted in Figure 2.1 with several polarization states mapped on it. These polarization states are explicitly defined in Section 2.2.4.
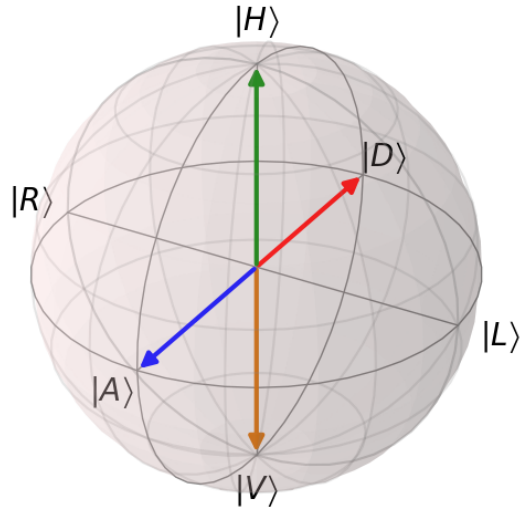
Figure 2.1: The Poincaré sphere, where antipodal points represent orthogonal states. The linear polarizations form a great circle, and the two pairs of orthogonal states H/V and D/A are indicated. These are the four states used in the BB84 protocol [BB14].

Alternatively, a polarization state can be described by the Stokes vector

$$\mathbf{S} = \begin{pmatrix} S_0 \\ S_1 \\ S_2 \\ S_3 \end{pmatrix}. \tag{2.2.13}$$

The Stokes parameters can be defined in terms of the electric-field description of equations (2.2.12).

$$S_0 = \langle A_x^2 \rangle + \langle A_y^2 \rangle \tag{2.2.14}$$

$$S_1 = \langle A_x^2 \rangle - \langle A_y^2 \rangle \tag{2.2.15}$$

$$S_2 = \langle 2A_x A_y \cos \phi \rangle \tag{2.2.16}$$

$$S_3 = \langle 2A_x A_y \sin \phi \rangle. \tag{2.2.17}$$

The component S_0 may be interpreted as the intensity of the light, while the S_1, S_2, and S_3 components represent the H, D, and R components of the polarization state [Hec17]. The degree of polarization DOP is given by

$$\text{DOP} = \frac{\sqrt{S_1^2 + S_2^2 + S_3^2}}{S_0} \tag{2.2.18}$$

and attains 1 for fully polarized light [Col04]. The Stokes parameters $(S_1, S_2, S_3)^T$ can also be interpreted together as the coordinates for a polarization state on a Poincaré sphere centered at the origin. Geometrically, the Stokes parameter S_0 is the distance between the point representing the polarization state and the origin of the Poincaré sphere. States such as those depicted in Figure 2.1 on the surface of the Poincaré sphere thus represent fully polarized light.

2.2.4 The qubit

The polarization degree of freedom can be written as a qubit. In the HV basis, the basis states are

$$|H\rangle = \begin{pmatrix} 1 \\ 0 \end{pmatrix} \qquad |V\rangle = \begin{pmatrix} 0 \\ 1 \end{pmatrix}. \tag{2.2.19}$$

The DA and RL basis vectors are written in the same basis as

$$|D\rangle = \frac{1}{\sqrt{2}} \begin{pmatrix} 1 \\ 1 \end{pmatrix} \qquad |A\rangle = \frac{1}{\sqrt{2}} \begin{pmatrix} 1 \\ -1 \end{pmatrix} \tag{2.2.20}$$

$$|R\rangle = \frac{1}{\sqrt{2}} \begin{pmatrix} 1 \\ i \end{pmatrix} \qquad |L\rangle = \frac{1}{\sqrt{2}} \begin{pmatrix} 1 \\ -i \end{pmatrix}. \tag{2.2.21}$$

The three pairs of orthogonal polarization states can be plotted on the Bloch sphere as qubit states. The states D, R, A, and L are plotted in Figure 2.1. Changes made to polarization states by an optical device can thus be visualized as operations on points on the Bloch sphere [KL10].

2.2.5 Optical devices

Polarization states may be rotated through variety of optical devices, passive and active. Passive devices include wave plates, pieces of birefringent material that induce a phase shift between the linear birefringent axes of light transmitted through it [Hec17]. These wave plates are typically made from quartz, and are carefully cut to particular thicknesses such that the net phase shift imparted on transmitted light is a half or quarter wavelength. Such wave-plates are accordingly referred to as half-wave plate (HWP) and quarter-wave plate (QWP) [HD88]. The polarization state of light may be controlled and adjusted through a sequence of wave plates, suitably adjusted to particular angles to implement the desired polarization rotation. In general, no more than three wave plates are required to implement an arbitrary polarization rotation [SM90].

Active devices are also used for polarization control. Such devices are utilize electro-optic media whose refractive index n varies as a function of the electric-field E applied across it. Depending on the material and voltages applied, this effect may be linear or nonlinear. The linear effect is known as the Pockels effect

and has the form

$$n(E) \approx n - \frac{1}{2}\alpha n^3 E, \qquad (2.2.22)$$

where α is the Pockels coefficient.

By controlling the direction and magnitude of the electric-field, the phase of transmitted light may be modulated. Such devices utilizing the Pockels effect in this way are accordingly known as phase modulators. Phase modulators are made from materials with substantial Pockels coefficient, such as lithium niobate ($LiNbO_3$). For a phase modulator of longitudinal length L, transverse faces separated by distance d, a voltage V applied in the transverse direction will induce a phase shift

$$|\Delta\phi| \approx \frac{\pi n^3 EL}{\lambda} \qquad (2.2.23)$$

on transmitted light of wavelength λ.

Phase modulators can be directly driven by electrical impulses and thus offer much higher switching rates, with modulation speeds up to the gigahertz range [Boy07].

2.3 Decoy state BB84

The first quantum communication protocol, BB84, was proposed by Bennett and Brassard in 1984 [BB14]. The protocol encodes quantum information in the polarization degree of freedom, in a sequence of states each modulated to one of the H, V, A, D polarizations. Without knowledge of the basis that any particular state was encoded in, an eavesdropper would not be able determine its polarization state without disturbing the signals, revealing their presence.

A direct implementation of BB84 using weak coherent pulses would open a security flaw, due to the possibility that some pulses will contain more than one photon. This makes a direct implementation vulnerable to the photon number splitting attack. Instead, the addition of decoy states may be used to implement QKD using weak coherent pulses [Hwa03; LMC05]. Such decoy states are identical to signal states in all aspects except for their average photon number. An eavesdropper thus cannot determine if a pulse was a signal or decoy state from a photon-number resolving measurement.

In the decoy state protocol, Alice may vary the intensity μ of the source coherent state $\left| \sqrt{\mu} e^{i\theta} \right\rangle$. The gain Q_μ and quantum bit error rate (QBER) are the weighted averages of the yield Y_n and QBER e_n of an n-photon signal,

$$Q_\mu = \sum_{n=0}^{\infty} Y_n e^{-\mu} \frac{\mu^n}{n!} \tag{2.3.1}$$

$$Q_\mu E_\mu = \sum_{n=0}^{\infty} Y_n e^{-\mu} \frac{\mu^n}{n!} e_n. \tag{2.3.2}$$

The yield and QBER are independent of whether a particular pulse was a signal or decoy pulse, leading to the following relations

$$Y_n(\text{signal}) = Y_n(\text{decoy}) = Y_n \tag{2.3.3}$$

$$e_n(\text{signal}) = e_n(\text{decoy}) = e_n. \tag{2.3.4}$$

The linear relations between Q_μ and Y_n, and between E_μ and e_n, allow Alice and Bob to estimate the yields Y_n and QBER e_n. In particular, the single-photon yield Y_1 and error e_1 may be estimated. The decoy-state method allows Alice and Bob to detect eavesdropping far more effectively, since any attack substantially perturbing the values of Y_n and e_n will be caught, provided that Alice and Bob have characterized their quantum channel well [LMC05; Xu+20].

Such decoy states can be readily implemented in practice using commercially available intensity modulators. One implementation of decoy-state BB84 is the use of three intensity levels – signal, decoy, and vacuum. The decoy state is set to be an intensity below the signal intensity, while the vacuum state has zero intensity. The sequence of intensity levels can be set by a quantum random number generator (QRNG).

2.4 Polarization maintaining fiber

Single mode (SM) fibers commonly used in optics do not preserve polarization states. External perturbations on the single mode fiber leads to mode coupling

between the two degenerate polarization modes, in effect applying a random unitary transformation to the polarization states of light passing through the fiber [Ras83].

Polarization-maintaining (PM) fiber was developed in part to preserve polarization state of light passing through the fiber, by preventing mode coupling within the fiber. This is done by introducing a large intrinsic birefringence within the fiber. The relationship between large birefringence and low coupling may be seen by considering the case of maximal mode coupling. Mode coupling is maximized when succesive perturbations induce coupling in phase, or when the spatial frequency of the perturbations κ are set equal to the spatial frequency of the fiber birefringence B

$$B = |\beta_x - \beta_y| = \kappa. \tag{2.4.1}$$

In general, the perturbations $\gamma(z)$ is a random function of z, the direction of wave propagation, with a zero average $\langle \gamma(z) \rangle = 0$. Moreover, the Fourier transform of $\gamma(z)$ gives the power spectrum $|\Gamma(\kappa)|$ which describes the power transfer between polarization modes as a function of spatial frequency. The function $\Gamma\kappa$ is a monotonically decreasing function, and therefore setting a cutoff spatial frequency κ_c where

$$\frac{|\Gamma(\kappa_c)^2|}{|\Gamma(0)|^2} = \epsilon \tag{2.4.2}$$

for some small ϵ will lead to a correspondingly small power transfer for

$$B \geq \kappa_C. \tag{2.4.3}$$

Empirically derived estimates of $\Gamma(\kappa)$ show that a beat length of $\sim$ 1mm will reduce power coupling by $\approx$ 40dB [Kam81; Buc04].

To attain the large birefringences necessary to produce a PM fiber, stress lobes can be introduced on either side of the circular fiber core. The stress lobes are doped such that their thermal expansion coefficients are altered while largely preserving its refractive index with respect to the surrounding cladding. During fiber fabrication, the stress lobes of the fiber preform cool at a different rate than the surrounding cladding, causing intrinsic stresses to form and in effect become frozen into the fiber. The resultant PM fiber birefringence is a combination of the

geometric asymmetric and intrinsic stresses due to thermal contraction [NOS86]

The PM fiber thus has two polarization eigenmodes, the fast and the slow axes. For a polarization-maintaining and absorption-reducing (PANDA) fiber [Shi+83], the slow axes passes through the two circular stress lobes, while the fast axes runs orthogonal to the slow axes. The typical birefringence for PM fiber is $\sim 10^{-4}$ [NOS86].

The fast and slow polarization eigenmodes spread in time as they propagate through PM fiber, causing a time delay $\Delta\tau$ between the arrival time of the two modes given by

$$\Delta\tau = \frac{BL}{c}, \tag{2.4.4}$$

where B is the PM fiber birefringence, L is the fiber length, and c is the speed of light. This delay is known as the differential group delay (DGD) [ST19]. To compensate for DGD, a series of PM fiber patch cords may be arranged with alternating fast and slow axes, such that signals propagate through equal distances aligned to the fast axis and slow axis [Pen+06].

2.4.1   Polarization drift

The PM fiber does not preserve all polarization states. Since its construction only prevents mode coupling, only the relative magnitudes of the light in the fast / slow axes of the fiber are preserved. In general, a state entering an PM fiber, written in the fast / slow basis

$$|\psi\rangle = \alpha \, |f\rangle + \beta \, |s\rangle , \tag{2.4.5}$$

will emerge from the fiber as the state

$$|\psi'\rangle = \alpha \, |f\rangle + e^{i\phi}\beta \, |s\rangle , \tag{2.4.6}$$

where ϕ is an additional phase factor due to the internal birefringence of the fiber and $|\alpha|^2 + |\beta|^2 = 1$. Polarization states trasmitted in PM fiber are therefore constrained to a circle on the Poincaré sphere. This is in contrast with SM fiber, where states may evolve arbitrarily on the Poincareé sphere due to mode coupling.

The induced phase shift ϕ in PM fiber is related to its beat length L_B, which is the length of fiber which induces a 2π phase shift on propagating light. It is inversely proportional to the fiber's birefringence and is given by

$$L_B = \frac{\lambda}{B},\qquad(2.4.7)$$

where λ is the wavelength of light and B is the birefringence of the fiber [NOS86].

For applications where only a single polarization needs to be preserved, light may be coupled into either axes of the fiber. However, an implementation of BB84 relies on polarization encoding in non-orthogonal states, and therefore directly preserving the polarization states of all four polarization states simultaneously is impossible.

In addition, the birefringence of a PM fiber varies due to external factors, such as temperature changes and fiber motion [NOS86]. These factors cause an additional phase drift that varies in time, which must be monitored in real time and corrected to ensure accurate transmission of polarization states.

2.5 QEYSSat

Fiber-based quantum communication is limited by the exponential losses within fiber. Although commercially available optical fibers experience relatively low losses of $0.2\mathrm{dB\,km}^{-1}$ [Yan+12], the channel losses limits communication to the hundreds of kilometers, depending on the protocol used [Pir+20]. Optical amplifiers such as those used for classical communication cannot be used for quantum communication, since direct amplification of quantum signals amounts to quantum cloning [Sca+05]. Quantum repeaters can overcome this limit on ground-based fiber quantum communication and is an active area of research, though such technology remains in development [Mun+15]. Moreover, the theoretical repeaterless bound for QKD is given by the Pirandola-Laurenza-Ottaviani-Banchi (PLOB) bound of $-\log_2(1-\eta)$ bits per channel used. This corresponds to $\approx 1.44\eta$ in the high loss regime, where η is the transmissivity of the channel.

Satellite-based links can be used to extend the distance of quantum links – losses in free-space communication scale quadratically and thus allow for longer links. This scaling arises from the increasing beam radius as a Gaussian beam prop-

agates through free space and is referred to as geometric loss [And06; PLA03]. One constraint associated with satellite links is atmospheric loss, which can absorb over 90% of transmitted signals at certain wavelengths. Wavelengths must therefore be chosen to maximize atmospheric transmission. Possible satellite link wavelengths are the transmission windows near 780nm and 1550nm, which can allow for greater than 40% and 70% transmission through the atmosphere near zenith angles, respectively [Bou+13]. Although the 1550nm window would be suitable for integration with existing telecom infrastructure, the lower efficiency and performance of semiconductor detectors at this wavelength restrict their use in quantum communication [Mig+13].

The Quantum EncrYption and Science Satellite (QEYSSat) mission is a science demonstration mission funded by the Canadian Space Agency (CSA) to demonstrate QKD from space [Jen+14], planned for launch in 2025 [Can23]. The demonstration includes a satellite uplink to be established with a weak coherent pulse source (WCPS) and an entangled-pair source (EPS), both producing quantum signals near 780nm. The WCPS will perform QKD using the decoy-state BB84 protocol, while the EPS will perform QKD using the BBM92 protocol. Using the QEYSSat satellite as a trusted node, a secret key can be established between ground stations separated by more than 400km at the University of Waterloo and CSA in Saint-Hubert, Quebec [Sco+20].

Chapter 3

Weak coherent pulse source

The weak coherent pulse source (WCPS) prepares polarization- and intensity-modulated photon states for decoy state BB84 and will be one of the photon sources to demonstrate a QKD uplink to QEYSSat. Pulses generated by the WCPS in the laboratory are brought to a rooftop transceiver telescope through PM fiber, to be transmitted to QEYSSat during a satellite pass. The transceiver telescope acts as both the transmitter for the quantum signal and also the receiver for a classical downlink from the satellite, used for APT.

PM fibers are used throughout the WCPS and fiber links of the ground station. In order to minimize the impact of differential group delay (DGD) from PM fiber, optical pulses must travel an equal distance along the fast and slow axes of the PM fiber. Therefore, matching fiber lengths and alignment of fiber axes is crucial to minimizing the quantum bit error rate (QBER) associated with the WCPS. A wave packet model was developed to compute tolerances on fibers lengths and angular alignment and is discussed in Section 3.3.

3.1 Weak coherent pulse source

3.1.1 Block diagram

The weak coherent pulse source (WCPS) consists of a 780nm pulsed laser source, an intensity modulation assembly, and a phase modulation assembly. An arbitrary waveform generator (AWG) produces the electrical inputs to the pulsed laser and

modulation assemblies, describing the sequence of intensities and polarization states required for decoy state BB84. Polarization-maintaining (PM) fibers are used throughout the source; PM fiber can also be used to carry the quantum signals to the ground station transceiver telescope. A block diagram of the WCPS is shown below in Figure 3.1.
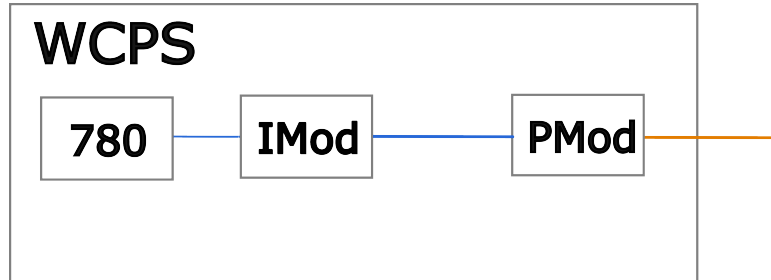
Figure 3.1: Block diagram of the WCPS assemblies. The pulsed laser assembly, described in detail in Figure 3.2, produces linearly polarized light at 780nm which are fiber-coupled into SM fiber (blue). The intensity modulation assembly (IMod) sets the decoy state intensities, while the phase modulator (PMod) assembly sets the polarization encoding and is described in detail in Figure 3.3. The WCPS output is the intensity- and phase-modulated weak coherent pulses, coupled into PM fiber (orange) to be carried to the transceiver telescope for a satellite uplink.

3.1.2   Pulsed laser source

The pulsed laser source produces coherent pulses at 785nm, where the wavelength was selected in part to take advantage of lower atmospheric absorption around this wavelength [Bou+13]. The current laser source uses sum-frequency generation (SFG) between a continuous-wave (CW) 1590nm laser source and a pulsed 1550nm laser source. The source is fiber based and the output is coupled into a single-mode fiber, shown in Figure 3.2 below.

Pulsed source
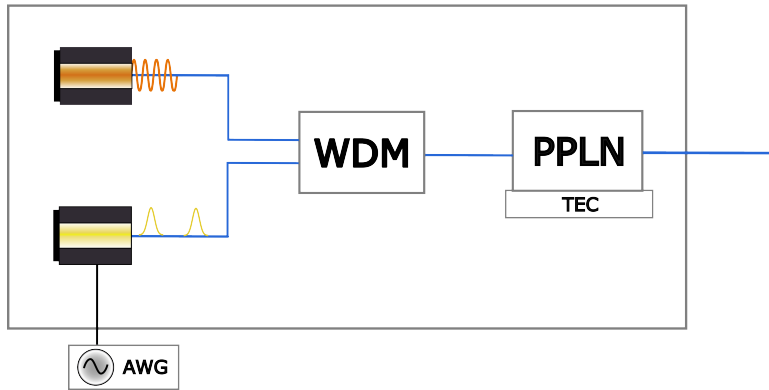
Figure 3.2: The pulsed laser source assembly uses a CW 1550nm laser (orange) and a pulsed 1590nm Q-switching laser (yellow), whose outputs are combined at a wavelength division multiplexer (WDM). The pulsed laser is driven at 400MHz by an electrical pulse from an arbitrary waveform generator (AWG), which controls the pulse frequency and duty cycle. Frequency conversion is performed through SFG using a magnesium-oxide doped periodically poled lithium niobate (PPLN) crystal, whose temperature is tuned using a thermoelectric cooler (TEC) to produce an output near 785nm. The CW laser is an EMCORE TTX1994 Integrable Tunable Laser Assembly and the pulsed laser is an ID Quantique ID300 short-pulse laser source.

3.1.3   Intensity modulation assembly

The intensity modulation assembly sets the relative amplitudes of each pulse to generate the signal, decoy, and vacuum states. Attenuators can be added to reach the desired intensity of the signal and decoy state, which are set to be $|\alpha| < 1$ to ensure security. The intensity modulator is a commercial off-the-shelf device comprised two phase modulators set in a Mach-Zehnder interferometer (MZI) configuration, whose relative phase is tuned to control the intensity of the output coherent state. The signal and decoy state intensities are driven by an AWG input, while the vacuum state intensity modulation can be performed by directly suppressing the electrical pulse driving the pulsed laser in the pulsed laser source.

The weak coherent pulses must be at the desired intensity at the exit of the weak coherent pulse source; attenuators may be placed in the intensity modulator assembly or within the free-space bridge of the phase modulation assembly to obtain the correct intensities. To monitor the intensity levels of the signal, decoy,

18

and vacuum states, a fiber-based beam splitter is used as an intensity pick-off within the WCPS. This splitter is placed at end of the phase modulation assembly, at the end of the WCPS.

3.1.4 Phase modulation assembly

The phase modulation assembly sets the polarization states of the weak coherent pulses for the BB84 protocol. The polarization encoding of the protocol uses the H, V, A, D polarizations. However, the polarization eigenmodes of the PM fiber are linear polarizations, and thus pulses are encoded and transmitted through the PM fiber of the WCPS and Quantum Optical Ground Station (QOGS) as the D, R, A, L polarizations. The polarization states are rotated from the DRAL circle to the HVAD circle within the transceiver telescope of the ground station, prior to transmission to QEYSSat.

The assembly consists of two phase modulators. This allows the phase shift to be performed in two steps so that the maximum phase shift performed by either modulator is halved (from $3\pi/2$ to $3\pi/4$), reducing the voltage switching requirements of the electrical input driving each modulator.

The phase modulators are fiber-coupled with the input polarization state set to $|D\rangle$. The polarization encoding is performed by setting the $|D\rangle$ state to the states $\{D, R, A, L\}$, each spaced $\pi/2$ apart. Since they lay on the same great circle on the Poincaré sphere, they can be seen as varying phase shifts on the input polarization state. The general output state can be parametrized using the variable ϕ, written as

$$|\phi\rangle = \frac{1}{\sqrt{2}}(|H\rangle + e^{i\phi}|V\rangle), \qquad (3.1.1)$$

where $|H/V\rangle$ are the slow/fast axes of the PM fiber and $\phi = \{0, \pi/2, \pi, 3\pi/2\}$ correspond to the $\{D, R, A, L\}$ states, respectively. Tuning a $\phi/2$ phase shift at each of the two phase modulators produces the four states required by the protocol.

The birefringence within the PM fiber and lithium niobate phase modulators themselves also leads to differential group delay (DGD) between the fast and slow modes as signals propagate along the assembly. To minimize the total DGD within the system, the axes of the first phase modulator and PM fibers in the first half

of the assembly is flipped relative to the axes of the second phase modulator and
PM fiber in the second half of the assembly, where the total length of PM fibers
aligned to either axis should be made as close to equal as possible. The impact
of differential group delay on QBER is investigated and quantified in the wave
packet model, discussed in detail in subsection 3.3.
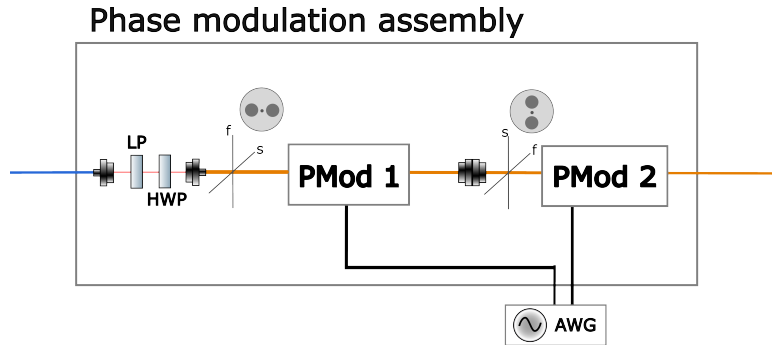
Figure 3.3: A free space bridge is placed at the entrance of the phase
modulator assembly, with a linear polarization (LP) to ensure linear
polarized input to the assembly, and a HWP to set a $|D\rangle$ input.
The phase modulator assembly consists of two PM fiber pigtailed
EOSpace phase modulators, both of the same model, connected in
series. The fiber axes are switched at the fiber connection between
the two phase modulators, coupling the fast axis to the slow axis and
vice versa. The phase modulators are driven by an AWG.

The AWG output is also amplified by an RF amplifier (not shown) to reach the
voltage levels required to induced the necessary phase shifts. Since the fiber
axes are switched between the phase modulators, the second phase modulator is
driven by a signal of opposing sign compared to driving signal to the first phase
modulator. An intensity pick off (not shown) is also placed at the exit of the
second phase modulator, to monitor the intensity levels of the signal, decoy, and
vacuum states at the output of the WCPS.

Additional components may be added to the free space bridge as required. A
bandpass filter can be added to ensure that only the desired quantum signal
around 785nm remains after the frequency conversion from telecom wavelengths,
and free-space attenuators can also be added to achieve the required average
photon intensities of the signal and decoy states. The free-space bridge within the
assembly also allows additional wave plates to be inserted, making this a potential

location for a polarization control system.

3.1.5   Quantum optical ground station

During operation of the Quantum Optical Ground Station (QOGS), the quantum sources will be housed within the indoor laboratory at the University of Waterloo Research Advancement Center (RAC). An optical fiber link will carry the quantum signals to the rooftop transceiver telescope to be transmitted to QEYSSat during a satellite pass. The optical fiber link may be a single-mode fiber or a polarization-maintaining (PM) fiber. A PM fiber link has the advantage of simplifying polarization control to a single phase parameter, further discussed in chapter (5). In the case of a PM fiber, a PM fiber link to the transceiver telescope should also include two segments of equal length with alternated axes to minimize differential group delay.
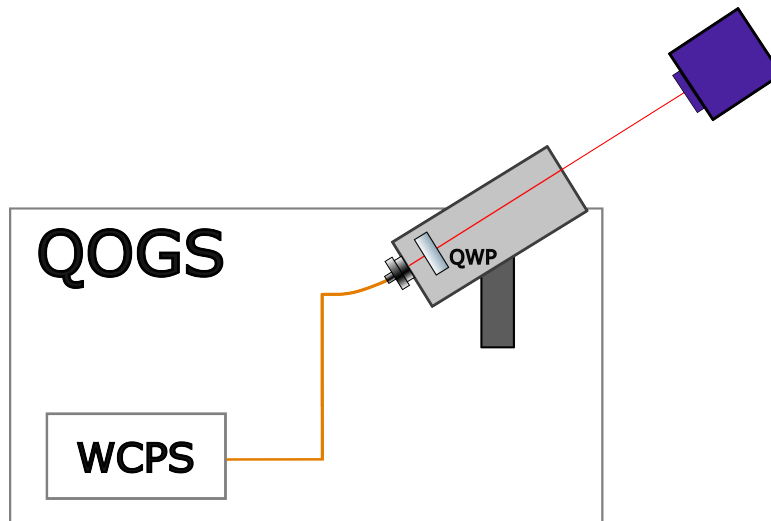
Figure 3.4: The WCPS is held in the RAC laboratory, before passing through a PM fiber link of roughly 50m length to reach the transceiver telescope on the rooftop. The $\{D, R, A, L\}$ polarization states carried within PM fiber are rotated to the $\{D, H, A, V\}$ states with a quarter-wave plate (QWP) within the transceiver telescope, just prior to transmission to QEYSSat.

The QWP may be incorporated into the acquisition, pointing, and tracking (APT) system of the telescope, responsible for exchanging beacon laser beams between the ground station and satellite to maintain a continuous quantum communication

link during a satellite pass.

3.1.6 Polarization-maintaining fiber and phase drfit

Polarization-maintaining (PM) fiber is used in the WCPS and can also be used in the fiber link to the transceiver telescope. The large internal birefringence of the fibers constrains polarization states to maintain the ratio of their field amplitudes in the fast and slow axes.

The birefringence of the fiber is sensitive to external perturbations, including temperature and mechanical stresses, and vary as outdoor temperature fluctuate and as the connected optical fiber moves while it tracks QEYSSat. Therefore, phase changes are induced on quantum signals carried within the fiber during QOGS operation. This phase shift φ is applied on all four polarization states equally, bringing the desired quantum states $|\phi\rangle$ to $|\phi'\rangle$.

$$|\phi'\rangle = |H\rangle + e^{i(\phi+\varphi)} |V\rangle , \qquad (3.1.2)$$

where $|\phi'\rangle$ are the uncorrected states exiting the transceiver telescope. Additionally, phase drifts will accumulate over the course of a day due to the fiber exposure to outdoor temperature conditions. In order to ensure frame alignment between Alice (the WCPS) and Bob (QEYSSat), the quantum signals must be brought back to $|\phi\rangle$ by a polarization control system. This will be discussed in chapter (5).

A polarization pick off is used to monitor the phase modulated pulses. The polarization pick off is placed at the aperture of the transceiver telescope, described in subsection 3.1.5, to monitor both the relative phase between the four distinct polarization states from the phase modulation assembly, and the overall phase shift induced by birefringence changes within the PM fiber of the WCPS and fiber link to the transceiver telescope. This allows the system to be calibrated so that two pairs of mutually orthogonal states are produced by the phase modulation assembly, and for active polarization control to be performed so that the outgoing states at the transceiver are in the H, V, A, D polarizations. The issue of phase drift is further discussed in chapter .

3.2 Pulsed laser source

3.2.1 Spectrum

The spectrum of the pulsed laser assembly output was measured using the Anritsu MS9710B optical spectrum analyzer.
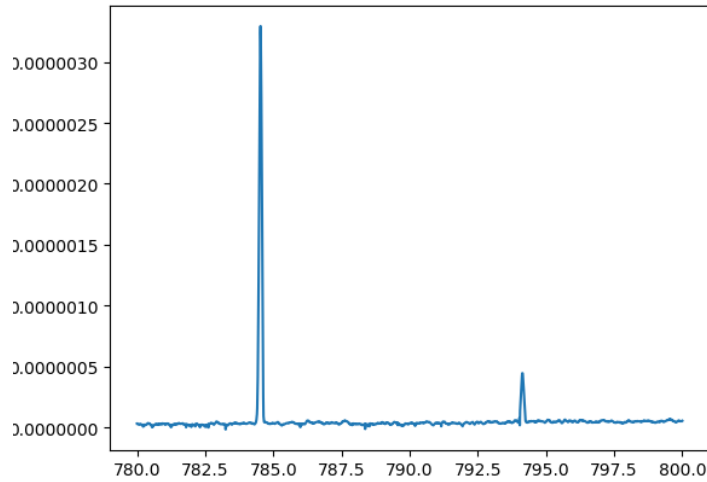
Figure 3.5: The spectrum of the pulsed laser, as measured by the Anritsu spectrometer. A secondary peak from the pulsed laser assembly is present near 795nm

Given the presence of a secondary peak near the intended 785nm output, a narrow bandpass filter should be placed in the free space bridge at the phase modulator assembly entrance to remove it.
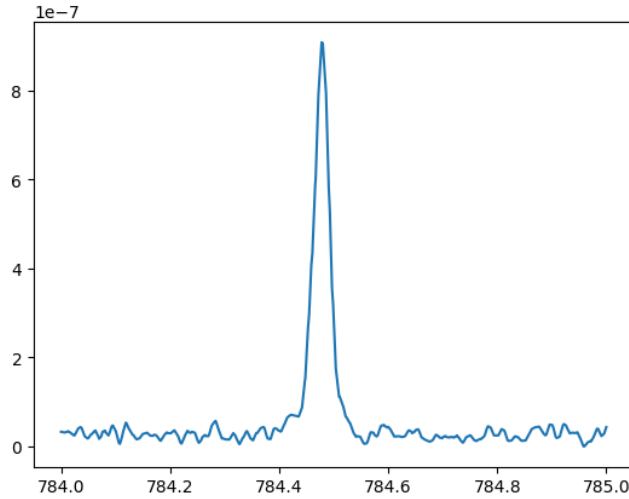
Figure 3.6: The main peak from the spectrum analyzer, zoomed in to determine the spectral width.

The laser pulses are seen to have a spectral width of roughly 0.1nm. The wavelength is near 785nm to take advantage of the lower atmospheric absorption in that wavelength range.

3.3 Wave packet model

One particular concern in using PM fiber is the accumulated differential group delay (DGD) when transmitted pulses contain components in both polarization eigenmodes of the PM fiber. A solution is to use two sets of PM fiber segments with the same total length, where the fast / slow axes of one set of segments is aligned to the slow / fast axes of the other set of segments [God+22]. The total DGD at the output of the WCPS will be close to zero, provided that the fiber lengths have been accurately matched.

Another issue is accurate angular alignment at fiber joints when aligning the fast axis of one fiber segment to the slow axis of the next fiber segment. In the idealized case, each of the four polarization encoded states $|D\rangle$, $|R\rangle$, $|A\rangle$, $|L\rangle$ will evolve in a great circle on the Poincare sphere parametrized by a single phase parameter ϕ, as

$$|\phi\rangle = |H\rangle + e^{i\phi} |V\rangle, \tag{3.3.1}$$

24

for some value of ϕ, as it travels along the PM fiber. However, an angular misalignment will cause light to be coupled into PM fiber with a state of slightly unequal magnitudes in its two polarization axes, causing it to no longer evolve along a great circle. Rather, they would evolve along a small circle of form

$$|\phi_\epsilon\rangle = \sqrt{1-\epsilon}\,|H\rangle + \sqrt{1+\epsilon}\,|V\rangle. \tag{3.3.2}$$

The impact of angular misalignment is depicted in Figure 3.7.
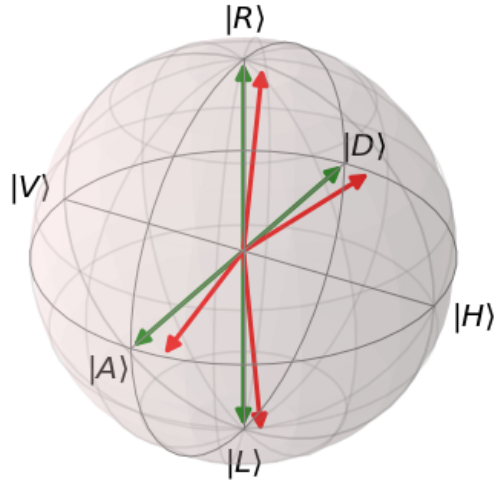
Figure 3.7: A state aligned in an equal superposition to the fast and slow axes of a PM fiber will evolve along a great circle, passing through the circular polarizations, as is the case in the diagram if $|D\rangle$ were coupled into the fiber. This state $|D\rangle$ will evolve to $|H\rangle$, $|A\rangle$ and $|V\rangle$ (green, in the figure). If the linear polarization were slightly misaligned with the PM fiber axes, it will be coupled as the state $|D_\epsilon\rangle$ with some angular error ϵ on the Poincare sphere twice that of the physical angular misalignment. The state $|D_\epsilon\rangle$ will travel along a small circle to $|R_\epsilon\rangle$, $|A_\epsilon\rangle$, $|L_\epsilon\rangle$ (red vectors in the fiture), thus never reaching either circular polarization.

Such a misaligned state will impact the final QBER of the states produced. For example, the $|D_\epsilon\rangle$ state is no longer orthogonal to the $|A_\epsilon\rangle$ state, so they are no longer perfectly distinguishable.

Due to the use of polarization encoding, this process happens concurrently for all

four polarization states, which will all evolve along slightly different circles for a given angular misalignment at a fiber joint, and at every misaligned fiber joint thereafter. This makes restoration of the polarization states to the desired states complex compared with polarization control of a single polarization state, since all four states must be brought back to the $DRAL$ circle.

Since angular misalignment and length differences are unavoidable in any implementation, a wave packet model was developed to quantify the acceptable tolerances so that the WCPS can produce states suitable for the QEYSSat uplink.

3.3.1 Model

The wave packet model considers the case of a $|D\rangle$ state injected into two PM fiber segments with its axes rotated by 90° relative to the other fiber. In ideal circumstances of equal length fibers and perfect angular alignment, H/V will be aligned exactly with the slow/fast axes, the total differential group delay will be zero and the outgoing state will be a pure polarization state $|\phi\rangle = |H\rangle + e^{i\phi}|V\rangle$ with fast / slow components of equal magnitude. This state be brought back to the $|D\rangle$ by appropriate adjustment of ϕ. Physically, this can be done with in-line polarization controllers such as an fiber squeezer controller.

However, any length mismatch will cause the pulse to emerge from the fiber segments with fast / slow components that are still separated, and so portions of the fast / slow components have no temporal overlap. Any angular mismatch will cause the outgoing state to have fast / slow components of differing amplitudes, creating a outgoing state $|\phi_\epsilon\rangle = \alpha|H\rangle + e^{i\phi}\beta|V\rangle$ (where $\alpha \neq \beta$), making it impossible to bring the state back to $|D\rangle$ through adjustment of the phase ϕ.

The goal of the model is to understand the relative impact of length mismatches and angular misalignments in the WCPS, and quantify the tolerance of either error that can be present in the WCPS while still producing states with a sufficiently low QBER.

The wave packet model was implemented in Mathematica. The input $|D\rangle$ pulse is defined as a sinusoid with an envelope of equal amplitude in both the H and V components. At the first fiber joint, the angular misalignment θ_1 causes the input polarization state to become a linear polarization slightly offset from $|D\rangle$. As the pulse travels through the first PM fiber of length L_1, a differential group delay of

26
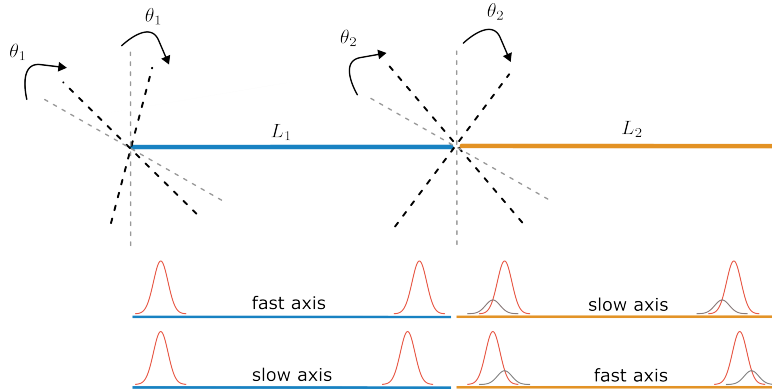
Figure 3.8: The two fiber segments of the wave packet model. The first and second fibers have lengths L_1 and L_2, respectively. H/V is defined in the laboratory frame, while the PM fibers are aligned to the lab frame with angular errors θ_1 and θ_2. The first fiber has its slow/fast axes aligned to H/V and the second fiber has its fast/slow axes aligned to H/V, respectively. The model injects $|D\rangle$ (defined in the lab frame) into the two fibers. In the ideal case of $L_1 = L_2$ and $\theta_1 = \theta_2 = 0$, the output state will also be a $|D\rangle$.

$\Delta t = BL_1/c$ is accumulated. This causes the pulse to separate in the first fiber segment. The pulse is treated as a monochromatic pulse.

At the second fiber joint, the angular misalignment between the first and second fiber segments ($\delta\theta = \theta_2 - \theta_1$) creates secondary pulses. The component in the fast axis of the first fiber mostly couples into the slow axis of the second fiber (the red envelope in 3.8), but a small portion (proportional to $\sin(\theta_2 - \theta_1)$) couples into the fast axis (the grey envelope in 3.8). The same occurs for the slow axis component, so two secondary pulses are created. The secondary pulses are also referred to as the "ghost" in literature [Pen+06].

The second PM fiber of length L_2 induces differential group delay of $\Delta t = BL_2/c$, recombining the primary (red) pulses. As the primary pulses recombine, the secondary pulses further separate. Each successive fiber joint creates more secondary pulses; this slowly degrades the visibility of the output state and is sometimes referred to in literature as visibility fading [Nak+23].

The recombined pulse will be a state that has near ideal temporal overlap between the fast / slow components at the end of the second PM fiber, with nearly equal amplitudes between the fast / slow components. As a measure of QBER, the

27

visibility of the outgoing state is computed.

In the lab, this is measured by setting a linear polarizer at the WCPS output to the $|D\rangle$ polarization, and then tuning the phase ϕ of the transmitted state to obtain a maximum and a minimum at a detector placed past the polarizer. The maximum should be a state close to $|D\rangle$ and the minimum should be a state close to $|A\rangle$. The visibility is calculated as

$$\mathcal{V} = \frac{I_{\max} - I_{\min}}{I_{\max} + I_{\min}}, \tag{3.3.3}$$

where $I_{\max}$ represents the projection I_D onto $|D\rangle$ and $I_{\min}$ represents the projection I_A onto $|A\rangle$.

In the wave packet model, the two primary pulse components of the state exiting the second fiber segment are set to be in phase with each other to produce a state close to $|D\rangle$, and out of phase with each other to produce a state close to $|A\rangle$. This is done by shifting either state by up to 2π, in analogy with the phase shift adjustment from a physical polarization squeezer applied to a PM fiber in the lab. The visibility for the output of the WCPS is computed the same way,

$$\mathcal{V} = \frac{I_D - I_A}{I_D + I_A}. \tag{3.3.4}$$

From the visibility, we can compute the QBER by the equation [Bou+13]

$$QBER = \frac{1 - \mathcal{V}}{2}. \tag{3.3.5}$$

In order to reach a QBER of 1%, the WCPS must produce states with a visibility of $\mathcal{V} = 98\%$. A QBER of 0.5% is obtained by a visibility of $\mathcal{V} = 99\%$.

The code used for the simulation is included in A, with plots illustrating the wave packets and underlying oscillations included on page A.4 of the appendix.

The wave packet model is performed with pulses of 300ps temporal width, similar to the output of the pulsed laser currently used in the WCPS. The wave envelope is a rectangular shape in order to simplify the numerical integration. From the temporal duration and spectral width of the pulse, the pulse is not Fourier limited. Moreover, the rectangular shape is still non-physical due to the sharp disconti-

nuities of the enveloped. Realistically, laser pulses will have a smooth curve in its rise time and fall time. Simulations using more realistic and refined envelope shapes is needed in future work.

3.3.2 Angular misalignment

The sensitivity of the visibility to angular misalignment at fiber joints is first investigated, by varying the angular misalignment at the fiber joint from $-3°$ to $+3°$. $|D\rangle$ polarized light is coupled into the first fiber segment with an angular error of $\theta_1 = +1.0°$ and $\theta_1 = +2.0°$ in two separate data runs, and a fiber length mismatch of 5cm is held constant through the simulation.
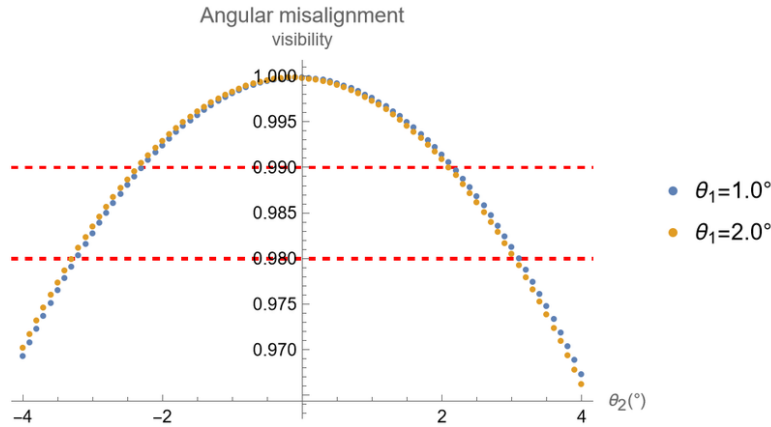
Figure 3.9: The output visibility is computed in $0.1°$ increments of θ_2, and the angular misalignment is seen to produce a quadratic-like loss in the visibility. Horizontal lines indicating $\mathcal{V} = 0.98$ and $\mathcal{V} = 0.99$ are drawn for reference.

The loss of visibility is very similar for both angular errors. The maximum visibility is slightly offset from $\theta_2 = 0°$, because perfect alignment at the fiber joint corresponds to $\theta_2 - \theta_1 = 0°$. In practice, it is easier to minimize both θ_1 and θ_2 separately. For the $\theta_1 = 1.0°$ simulation, $\mathcal{V} < 0.98$ when the misalignment angle $\theta_2 < -3.3°$ and $\theta_2 > 3.2°$, and $\mathcal{V} < 0.99$ when the misalignment angle $\theta_2 < -2.2°$ and $\theta_2 > 2.1°$.

3.3.3 Length mismatches

The length matching requirements for the PM fiber pair are investigated next, by fixing the angular alignment errors at $\theta_1 = +2°$ and $\theta_2 = -2°$ and setting a length mismatch of up to 25cm.
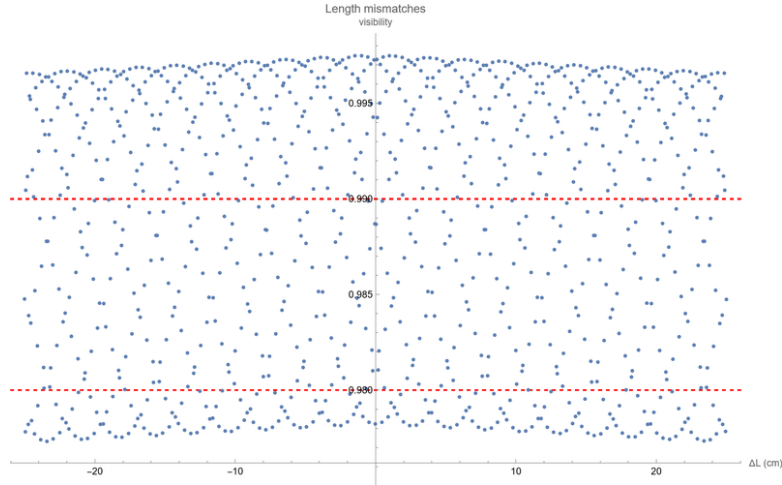
Figure 3.10: The length mismatches are incremented in 0.5mm steps, from 0cm to 25cm. Dotted lines for $\mathcal{V} = 0.98$ and $\mathcal{V} = 0.99$ are again indicated in red.

The crossing sinusoids are an aliasing effect. A plot showing a similar simulation with more fine-grained increments is shown in Figure (3.12). The visibility does show a trend of decreasing with increasing length mismatches, but an unexpected feature is that the visibility oscillates with a rather large amplitude at the millimeter length scale, causing a variation of visibility of almost 2%. Given that there is no way to accurately create a fiber patch cable to the submillimeter length scale, this seems to imply that for this given set of angular misalignment angles, there may be no possible length mismatch that one can practically achieve so that they produce states of $QBER < 1\%$.

The next plot in Figure (3.11) investigates the slowly decreasing visibiliy with increasing length mismatches, while the plot in Figure (3.12) investigates the aliasing effect and its origins.
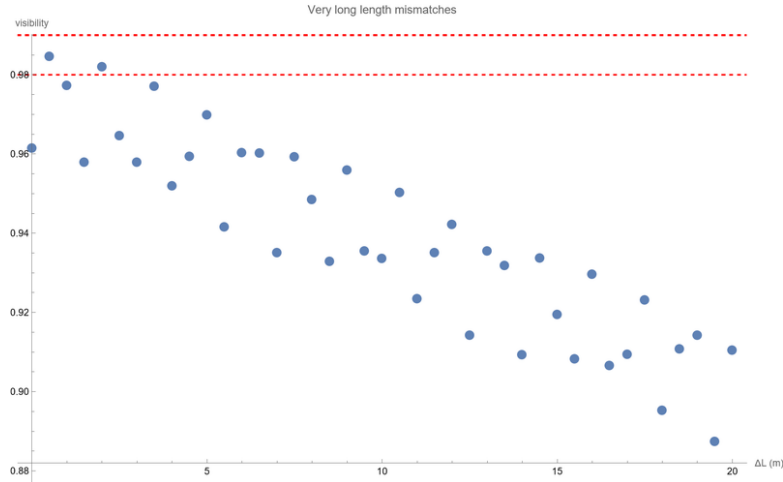
Figure 3.11: Another simulation was run with the length mismatches set up to 20m, using the same parameters as the simulation plotted in Figure 3.10.

The aliasing issue is seen again, with the visibility oscillating by about $\approx 2\%$ as the visibility decreases slowly to $\approx 90\%$ over a 20m length mismatch. Given the computation time of the simulation, mostly from the numerical integration of the field intensities, it was not feasible to compute the visibilities in small enough steps to avoid the aliasing issue.

This implies that the length matching is actually not a critical issue. The total length of fiber in the entire WCPS does not exceed several meters, and this potentially implies that length matching may not be necessary for the WCPS, given sufficiently long pulses and sufficiently accurate angular alignment in the fiber joints.

The aliasing issue in the previous two figures is investigated next. It was initially suspected that this may have been an issue with numerical stability. However, several checks of numerical stability, such as ensuring that computed results did not change appreciably by increasing the number of precision digits, seemed to imply that numerical accuracy was not the cause of the behavior. A plot from computing length mismatches in 0.1mm increments is included below.
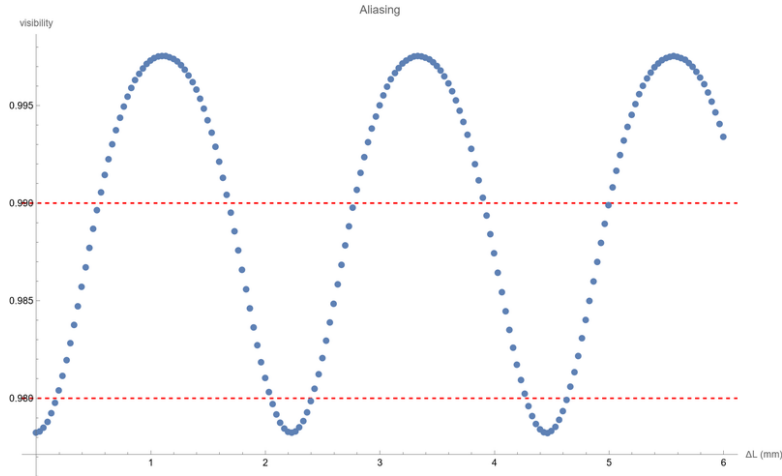
Figure 3.12: The length increments were decreased by a factor of 150 to increments of 1/30mm, for fiber length mismatches from 0 to 6mm.

The visibility follows a clear periodic pattern. It is similar to a sinusoid, though the troughs are noticeably narrower than the peaks. The periodicity lines up with the beat length of just over 2mm, and it was realized that the periodicity is coming from the interference between the secondary pulse produced at the fiber joint and the primary pulse that was injected into the fiber. The phase of the secondary pulse is determined by the exact length of the fiber as a multiple of the beat length, and may therefore constructively interfere with the primary pulse (the peaks of the curve) or destructively interfere with the primary pulse (the troughs of the curve).

This issue of destructive interference will be compounded in the WCPS, as there will be multiple fiber joints, each producing a set of secondary pulses that all act to destructively interfere with the primary pulse. The gradual loss of visibility is sometimes referred to as visibility fading in literature [Nak+23].

Another insight is that the ideal fiber length to minimize visibility fading is a half-integer multiple of the beat length. This is not directly feasible, but it may be possible to tune the effective optical path length of each fiber segment to be a half-integer multiple by attaching a fiber squeezer to each fiber segment.

Since it is not practically feasible to fabricate fiber patch cables to sub-millimeter accuracy, one way to assure a sufficiently high QBER is to minimize the amplitude

of the oscillations, by minimizing the angular error of each fiber joint. The next simulation considers the oscillation amplitudes for a given angular error in fiber alignment.
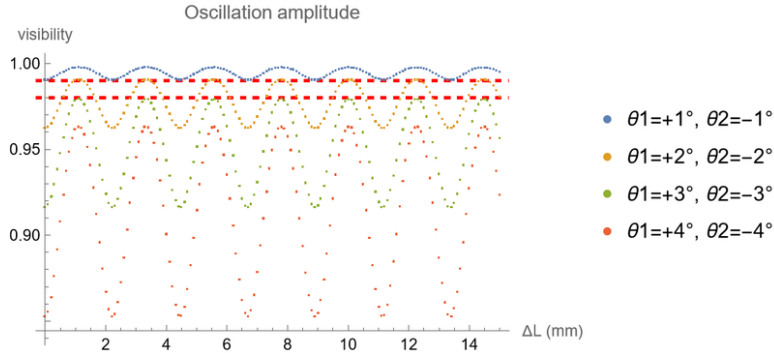
Figure 3.13: For a fiber alignment implementation capable of attaining an accuracy of θ', the maximum angle misalignment at a fiber joint is $2\theta'$, such as in the case that $\theta_1 = \theta'$ and $\theta_2 = -\theta'$. This simulation was run for fiber segments of $\theta' = \{1°, 2°, 3°, 4°\}$, while incrementing the fiber length mismatch in steps of 0.1mm.

One observation from this simulation is that the oscillation amplitudes do increase with angular aligment error. The amplitudes become quite substantial – for an alignment error of 4°, the visibility may vary by over 10% due to the destructive interference between the primary and secondary pulses.

Another observation is that the maximum visibility drops rapidly with angular alignment error. For a fiber connectorization implementation capable of reaching alignment errors of 2°, reaching a visibility of 99% is just barely possible. At a 4° error, the best possible visibility is just over 96%, corresponding to a QBER of 2%.
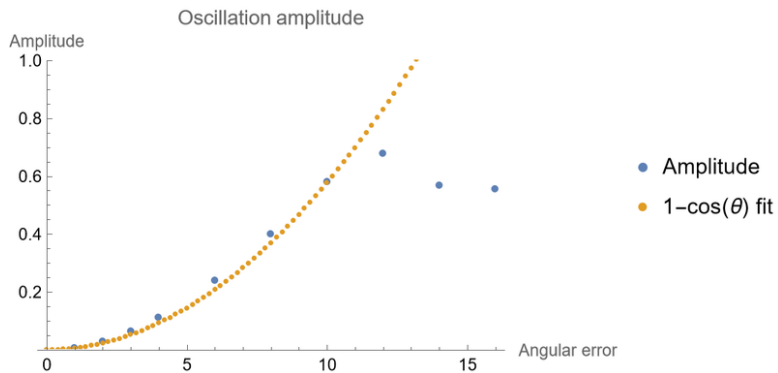
Figure 3.14: The simulation in Figure 3.13 was rerun for θ' up to $\theta' = 16°$. The oscillation amplitudes from the simulation were fit against an appropriately scaled $1 - \cos\theta$ function.

The amplitude of the oscillations is seen to rise quickly, following an approximately sinusoidal function as shown by the $1 - \cos\theta$ fit, though the exact form is likely complex and dependent on factors such as the wave packet envelope shape. Interestingly, the oscillation amplitude fall off and even appears to decrease for higher angular errors. Angular errors of such a large magnitude are unlikely to occur in a practical implementation, though they would be interesting to investigate.

3.3.4 Angular alignment target

Ultimately, the goal is to construct a WCPS with the smallest possible QBER. A simulation was run for targets that could realistically be obtained, using values for high levels of angular alignment reported in literature [Li+09].

34
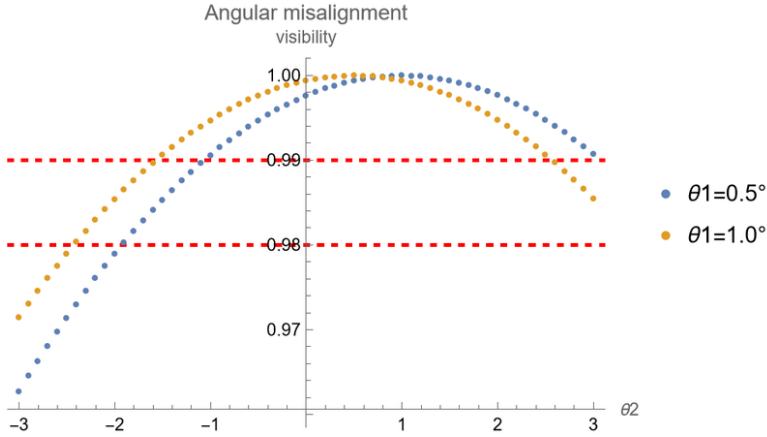
Figure 3.15: The simulation was rerun for a fiber length mismatch fixed at 2cm, with a set of data at an angular mismatch of $\theta_1 = 0.5°$ and another set at an angular mismatch of $\theta_1 = 1°$. The fiber joint angular mismatch is varied from $\theta_2 = -3°$ to $\theta_2 = +3°$.

The two plot are similar, with the maximum visibility attained for $\theta_1 = \theta_2$. The output visibility stays above 98% for a fiber joint angular alignment accuracy of 2%, and above 99% for a fiber joint angular alignment accuracy of 1%.

3.3.5 Shorter pulses

The wave packet model simulations was also repeated for much shorter pulses of 1ps duration, which may more accurately describe other photon sources, or a WCPS of a much higher repetition rate.

The wave packet simulation was run again for 1ps pulses, this time with a Gaussian envelope.
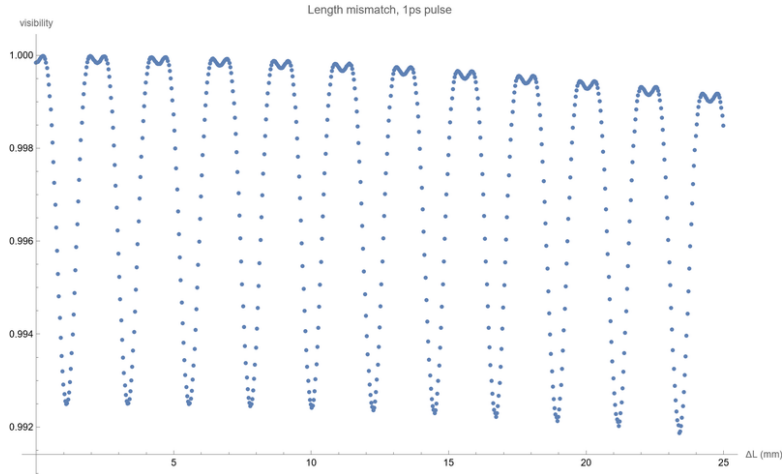
Figure 3.16: The simulation was run for a fixed angular misalignment of $\theta_1 = +2°$ when $|D\rangle$ light is injected into the first fiber, $\theta_2 = -2°$ denoting the angular alignment at the fiber joint, while output states were considered for length mismatches of up to 2.5cm, in 0.1mm increments.

The visibility is seen to decrease slightly for length mismatches on the centimeter scale even for the shorter 1ps pulses. The oscillations due to the varying constructive and destructive interference of the secondary wave packets can still be seen. Moreover, there is an asymmetry in the oscillations, where the visibility is seen to remain at the peaks over a greater range of length mismatches than the troughs. There is also a slight dip within the region of the oscillation peaks that is not seen in the simulation with the 300ps pulses performed with rectangular envelopes. Moreover, the peaks of the 300ps simulations in Figure 3.12 also appear to remain at the peaks over a slightly greater range of length mismatches as well. The asymmetry and structure of the feature will need further study to understand its origins.

The same simulation is plotted below in Figure 3.17 over a shorter range of length mismatches to show the visibility variation more closely.
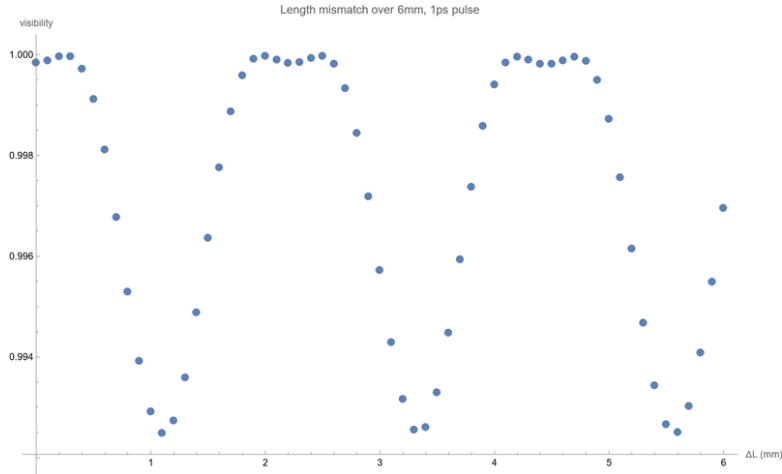
Figure 3.17: Wave packet simulation, performed for length mismatch increments of 0.1mm where $\theta_1 = +2°$ and $\theta_2 = -2°$.

The oscillations are shown to remain near the peak visibilities for a longer range of length mismatches, remaining near the peak for $\sim$ 0.5mm but only near the trough for $\sim$ 0.1mm. This behavior needs further study to understand its origins within the wave packet model.

Moreover, it can be observed that the visibility is gradually decreasing for increased length mismatches, as the envelopes become further separated after the imperfect DGD compensation. Therefore, it is still important to match the fiber lengths aligned to either axes. This is particularly for longer fiber links, such as the PM fiber link from the lab to the rooftop ground station.

3.3.6 Outlook

The wave packet model considers the case of two fiber segments with a single fiber joint. The angular mismatch was found to the dominant factor in impacting the visibility of the output states, while the length mismatch was not as important provided that the accumulated differential group delay is short compared with the pulse duration.

Moreover, this is a simplified model. The actual WCPS includes other birefringent elements, such as the phase modulators. It also includes multiple fiber joints, such as those between the phase modulators and the fiber patch cables connecting them. A more accurate model would be one extended to include multiple PM fibers and

birefringent elements.

The presence of multiple fiber joints would also produce multiple sets of secondary peaks, each destructively interfering with the primary pulse. The visibility fading from this process should be further investigated.

Another future step is to include a more realistic wave envelope, instead of the current rectangular and Gaussian wave envelopes. This may account for the rise and fall time of the laser pulse, and would depend on the particular laser diode used and how it is electrically driven. Another addition can be to include the spectrum of the laser pulse, which is currently simulated as a perfectly monochromatic beam. In reality, the laser pulse will have some finite bandwidth.

These additions will greatly benefit from more efficient method s of integrating the wave packet, which is currently a numerical integration of the individual oscillations through the entire wave packet.

3.4 Minimizing QBER

Further work needs to be done to minimize the QBER of states produced by the WCPS. From the wave packet model, the most critical variable is the angular misalignment at fiber joints. Although the fiber length matching is not as critical for the WCPS due to the relatively long pulse durations, any PM fibers connecting the RAC laboratory and transceiver telescope will have need differential group delay compensation with carefully length matched fibers, since other photon sources (such as an EPS) may have much shorter pulse durations.

Photon losses at fiber joints and within the system are not as critical, since the power level of the laser can be increased (the attenuation added within the WCPS can also be decreased). However, care must be taken to ensure that losses are not polarization dependent. Losses are best reduced by minimizing the number of connections in the system and by moving to fusion spliced connections where possible.

Two options for joining fibers were explored. A custom fiber connectorization set up was built to allow for alignment of the PM fiber axes. Alternately, fibers can also be fusion spliced.

3.4.1 Connectorizing fibers

Fiber connectorization of polarization-maintaining (PM) fibers requires rotational alignment of the polarization maintaining fibers. A custom in-house alignment system was developed, using a Carson USB microscope.

The connectorization of PM fibers starts with the same process as connectorization of single mode fibers. The optical fiber is threaded through the connector and epoxied into place. However, the key alignment requires that the PM fiber axes be aligned to the key slot. This alignment is typically done to either the fast or slow axis, though other alignments are possible.
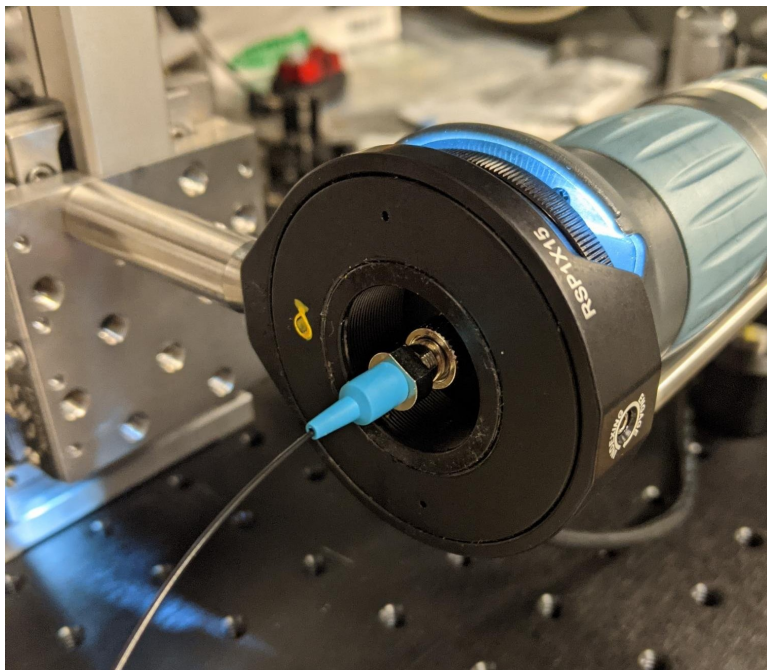
Figure 3.18: The in-house alignment system using the Carson zPix 300 USB microscope, whose 450× magnification allows the PM fiber endface to be imaged.

The PM fiber may be inserted into the holding mount. Alignment is performed optically by viewing images from the Carson microscope.
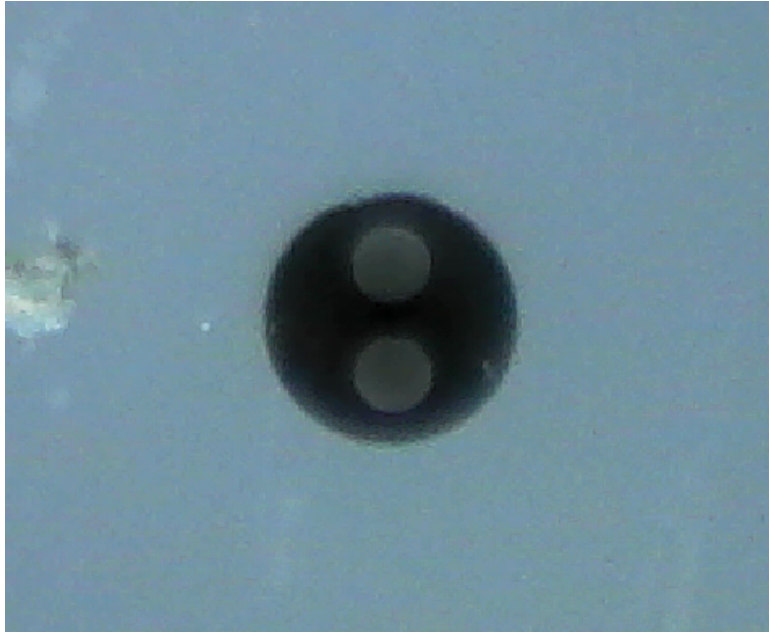
Figure 3.19: The endface of a PM PANDA fiber, used throughout the WCPS, imaged through the Carson microscope, showing the fast axis aligned to the horizontal and the sslow axis to the vertical.

The PM fiber alignment is performed using the Image Acquisition Toolbox in MATLAB, which detects the circles of the circular stress lobes of the PM fiber. Based on this, a horizontal and vertical angular alignment is computed. This allows for a more accurate alignment than relying on visual inspection.
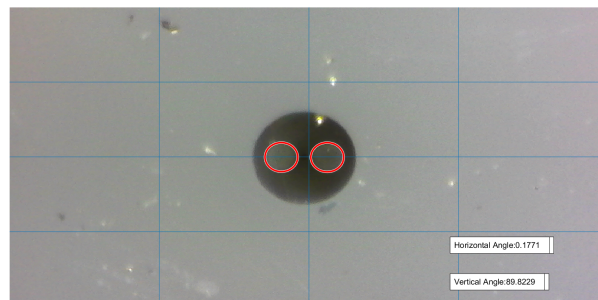
Figure 3.20: Screenshot from circle detection, showing the derived horizontal and vertical angles.

PM fiber patch cables connectorized for the WCPS were made using this alignment set up.

3.4.2 Splicing fibers

Another method for joining fibers is to use fusion splicing. This may be done with a fusion splicer such as the Vytran LFS4100 fusion splicing system [Tho], which contains an imaging system so fiber endfaces may be monitored, and stepper motors that allow for rotational alignment of fiber faces. A benefit of fusion splicing allows fibers to be joined with very low losses of ≈ 0.1dB [Hec93]. However, fusion splicing is a laborious process requiring costly equipment, and permanently fuses two fibers together. The permanent fusion may be a benefit in the case of rotational alignment, since a fiber joint will not lose its rotational alignment following splicing. However, in a system requiring modular components that may need to be replaced or modified, splicing fiber joints may not be a suitable solution.

Chapter 4

Phase drift

Polarization maintaining (PM) fibers are used in the weak coherent pulse source (WCPS) and Quantum Optical Ground Station (QOGS) so polarization control is reduced to a single degree of freedom. This degree of freedom can be written as the phase ϕ in the state $|\phi\rangle = \alpha\,|H\rangle + e^{i\phi}\beta\,|V\rangle$, taking α and β to be real and identifying the H and V modes with the fast and slow axes of the polarization maintaining fiber. In the BB84 protocol with ideal pulses, $\alpha = \beta = 1/\sqrt{2}$. The primary factors contributing to phase drift are examined to understand the phase drift expected during the operation of the WCPS and QOGS in a satellite pass.

4.1 Sources of drift

In PM fiber, states coupling into one of the two polarization eigenmodes remain in their respective eigenmode due to the large intrinsic birefringence of the fiber. However, the fiber birefringence varies due to environmental factors, including temperature changes and mechanical stresses. This alters the differential group delay (DGD) accumulated in PM fiber, which in turn alters the phase shift caused by pulses passing through the fiber. Since such variations are dependent on environmental factors, the exact phase drift is not constant and cannot be measured ahead of time. Instead, the phase of the state must be actively monitored during operation of the WCPS so that appropriate compensation can be carried out.

The main sources of phase drift are characterized to estimate a total expected phase drift. The dominant factors are temperature fluctuations and fiber motion.

The ambient temperature surrounding the fiber experiences large changes in the Canadian climate, particularly in the sections of the fiber in the ground station exposed to outdoor conditions. Large temperature fluctuations can appear through the course of the day depending to weather conditions. The other significant factor to phase drift is the motion of the fiber itself, since the fiber is attached to the transceiver telescope which must move to track the passing satellite.

The orientation of the satellite is an additional factor that influences phase control. The satellite orientation varies over the coarse of a pass, causing a frame misalignment where the polarization reference frame of the source on the ground does not agree with the reference frame of the receiver on the satellite. This frame misalignment affects the same degree of freedom as that caused by birefrigence changes in PM fibers, and can be corrected with the same polarization control system.

The intrinsic stresses of a PM fiber has been computed through both analytic and numerical means in early literature [NOS86]. However, the effects of external stresses to the internal birefringence of a fiber is more difficult to analyze. The exact effects to polarization remains dependent on many factors in a realistic setting, such as slippage due to coatings on a fiber and the method in which a fiber is held [KU81]. The sensitivity of polarization states passing through a PM fiber due to each individual factor should therefore be measured experimentally.

4.1.1   Temperature sensitivity

In a laboratory setting, temperature-dependent effects can be minimized by placing exposed fiber in thermally isolated enclosures. This is possible within the WCPS but impossible with the direct fiber link to the outdoor ground station. Therefore, the phase change from temperature changes must be characterized and compared with the outdoor temperature fluctuations expected in Waterloo in order to estimate phase changes arising from temperature changes.

To estimate the temperature sensitivity of PM fiber, a length of the fiber was immersed within an ice-water bath and allowed to equilibriate with the room temperature over several hours. During this time, polarized laser light was transmitted through the fiber and the phase shift induced by the temperature changes was monitored with a polarimeter. The temperature of the bath was also contin-

uously measured to extract a temperature-dependency in the fiber birefringence.
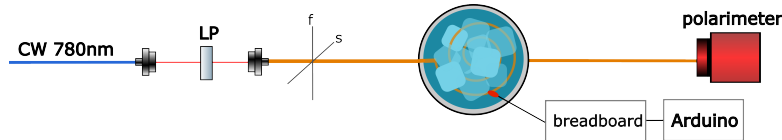
Figure 4.1: Light from a CW 780nm laser was coupled into free space, set to a $|D\rangle$ polarization and coupled into a 2m length PM fiber. 1.5m of the fiber is immersed in an ice water bath. To monitor the temperature, a thermistor and resistor was connected to an Arduino.
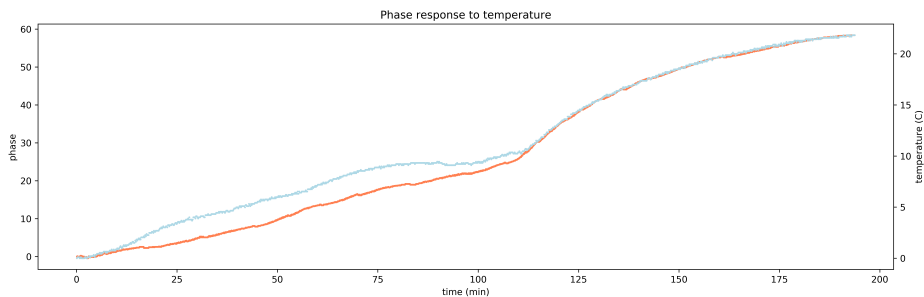
Figure 4.2: 1.5m of Thorlabs PM780-HP PM fiber was immersed and secured in an ice-water mixture. The starting temperature of 0°C equilibriated to room temperature over the course of several hours. The phase shift in radians (light blue) is plotted against the temperature rise (orange). Temperature readings were taken with a thermistor connected to an Arduino, while the phase shift was taken from measurements from a Thorlabs PAX1000IR1 polarimeter.

A nearly linear response is observed from approximately the 110 minute mark onwards, suggesting a direct proportionality between the temperature and phase response of a PM fiber. The more irregular phase shift observed within the first couple hours is likely due to the melting of the ice within the mixture, leading to an uneven temperature distribution within the bath. The uneven temperature distribution is also likely why a temperature induced phase response was observed even before all the ice had melted. Using the data from the ice-water bath after all ice has melted, a temperature-induced phase response was estimated to be $\Delta\phi = 1.8 \pm 0.6 \text{rad}\,°\text{C}^{-1}\,\text{m}^{-1}$, corresponding to a birefringence shift of approximately $\Delta B = 2.4 \times 10^{-7}°\text{C}^{-1}$. This measurement is consistent with results extrapolated from literature [Kys+17].

44

Weather station data

In Waterloo, a wide range of temperature conditions are expected, from $-40°$C to $+35°$C at the extreme ends, and the temperature swing over a 12 hour period can reach $20°$C. Although the temperature change over the course of a few minutes will be small, the large temperature changes over the course of days leads to a different absolute temperature-induced phase shift in the fibers, necessitating active monitoring and polarization control. The QOGS ground station contains a weather station to monitor conditions including local temperature, humidity, and irradiance. The temperature data collected for a winter month is plotted below.
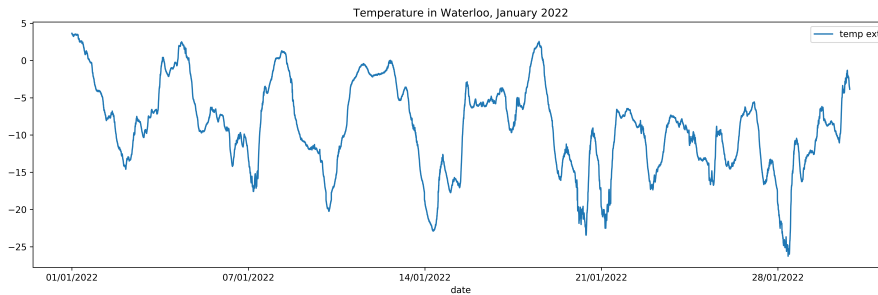
Figure 4.3: Temperature data collected from the QOGS weather station for the winter month of January 2022, showing fluctuations in temperature over the course of days.

4.1.2 Dynamic drift

A 50m PM fiber link takes the WCPS source output to the ground station telescope on the building rooftop. Mechanical stresses are exerted on the fiber throughout the link, particularly along the end connected to the moving telescope during a satellite during a pass. The combination of changing lateral, torsional, and bending forces changing the birefringence along different segments of the fiber, whose resulting phase shift is most easily estimated by direct measurement of similar motion.

A PM fiber was connected to the side of a telescope, which was then rotated at a fixed speed. The fiber was allowed to hang from the side of the telescope with some slack to prevent it from becoming taut during telescope motion, similar to how it would be set up in the ground station. This simulated the mechanical forces that the fiber would experience during a satellite motion. The results are

plotted below.
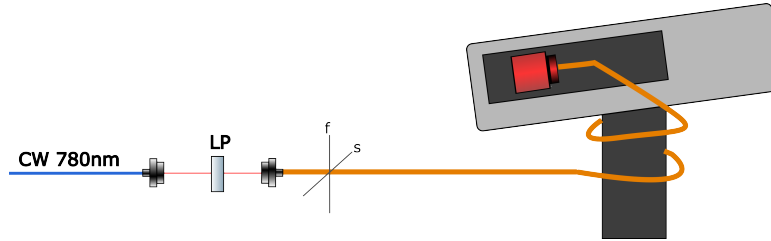
Figure 4.4: Light from a CW 780nm laser was coupled into free space, set to $|D\rangle$, before being coupled into PM fiber. The fiber was spooled around a telescope, and allowed to hang loosely. A Thorlabs PAX1000IR1 polarimeter was mounted to a breadboard near the end of the telescope for the dynamic test, so that it would move through a larger distance during the dynamic test.

The telescope used is longer in length than the transceiver telescope. Thus, the dynamic test would move the PM fiber through a further distance than would be expected during operation. The telescope was also moved at speeds substantially higher than those that would be expected during a satellite pass.
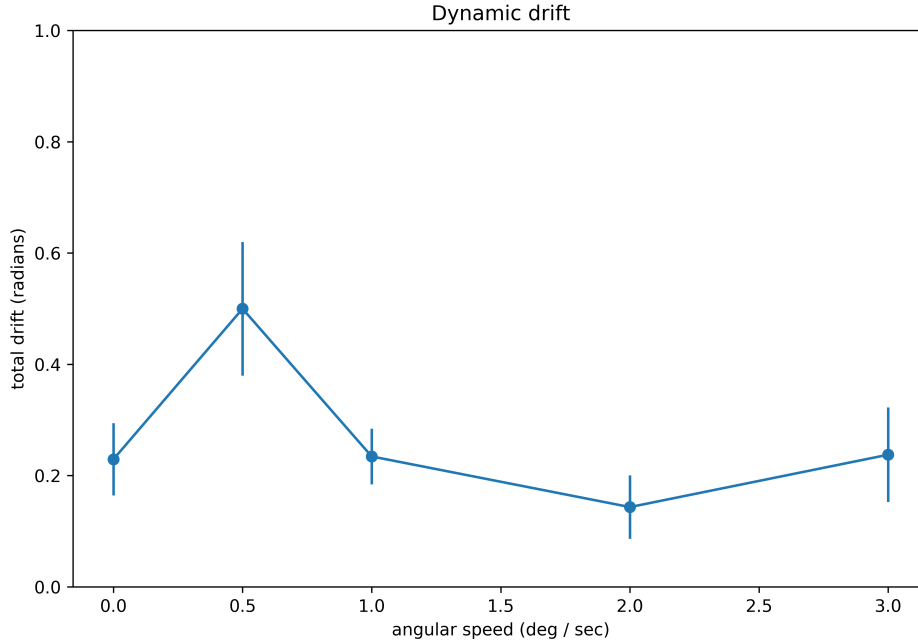
Figure 4.5: A PM fiber was connected to a Thorlabs PAX1000IR1 polarimeter mounted to one side of a telescope of similar length to the ground station telescope. The phase shift at a number of different angular speeds was measured as the telescope turned over a range of 66°. This included a measurement while the telescope was stationary to estimate the drift from a free-hanging fiber.

There did not seem to be a substantial connection between the rate of phase drift and the speed of telescope motion. The average phase shift over the measured range of motion was 0.27 ± 0.12rad. The range of motion here was only slightly over 60°, though a full satellite pass can involve telescope motion over close to 180°, increasing the total phase shift by a few factors.

4.1.3 Polarization stability

The phase drift induced by a PM fiber drifts over time, in some combination of hysteresis effects of previous stresses on the fiber and external environmental influences such as temperature changes and vibrations. These cause a slowly varying phase drift. To estimate the degree of the effect, the phase of a length of PM fiber was measured while the fiber was laid at rest without any deliberately

applied stresses.
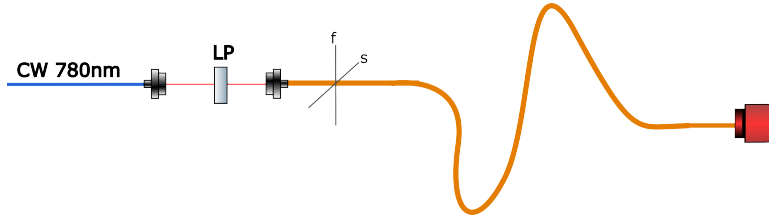
Figure 4.6: CW 780nm light set to $|D\rangle$ by a linear polarization (LP) is coupled into PM fiber, allowed to rest loosely on an optical table.
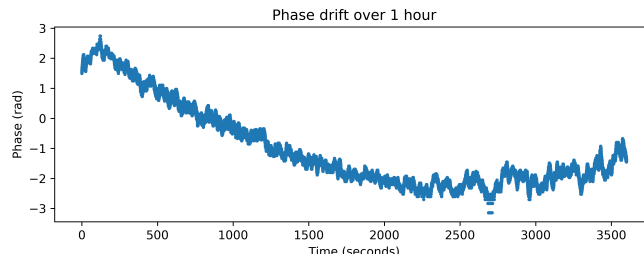
Figure 4.7: Phase drift over one hour for a 2m length of Thorlabs PM780-HP PM fiber, left to sit without disturbance on an optical table, measured with a Thorlabs PAX100IR1 polarimeter. The fiber was not taped down, since the fibers in the link between the WCPS and ground station will not be securely affixed to a surface. A fixed input polarization was passed through the fiber. The horizontal blip around the 2700s mark is a quantization effect due to the resolution of the polarimeter.

An Allan deviation plot was also produced as another measure of the phase stability within the PM fiber. For short measurement times of less than 10^{-1}s, the Allan deviation is slightly higher due to noise of the measurement instrument. The Allan deviation then steadily increases over time, as the phase within the fiber drifts. The minimum in Allan deviation also suggests an optimal measurement duration that measurements should be averaged over for best accuracy. For this device, this corresponds to averaging over approximately a quarter second.
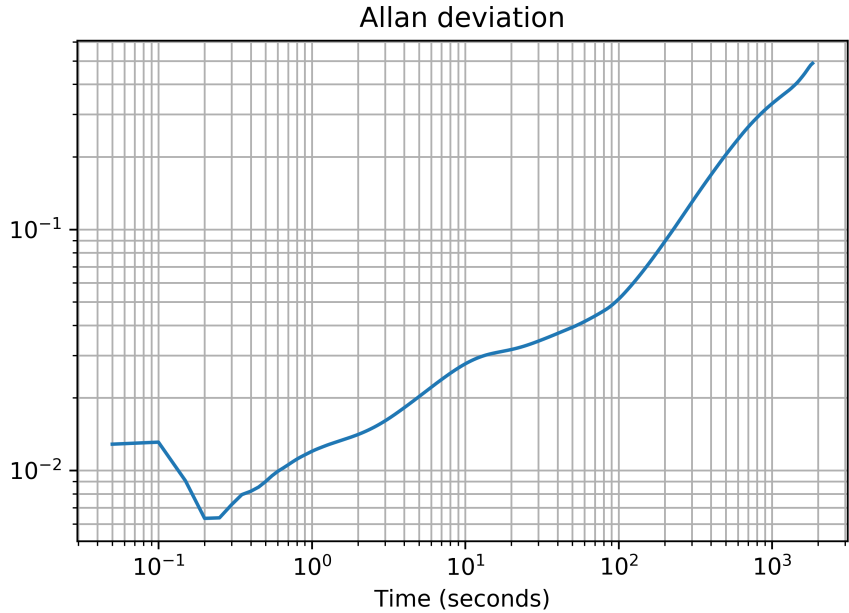
Figure 4.8: Allan deviation of the phase drift over an hour.

4.1.4 Satellite roll

Another factor that needs to be incorporated into the polarization control system is the frame misalignment that arises from the satellite orientation. Over the course of a pass, the satellite orientation changes, causing the reference frame of the measurement basis on the satellite to become misaligned with the reference frame of the basis when polarized pulses were produced at the source on the ground.

A misalignment in this reference frame causes the H and V basis vectors of the satellite to become oriented somewhere on the HVAD circle. Since this is the same degree of freedom effected by phase shifts within a perturbed PM fiber, it can be corrected using the same polarization control system. Information on the satellite orientation can be conveyed to the ground station using a polarized downlink beacon located on the satellite.

Separate orbit simulations of QEYSSat will be needed to estimate this quantity, since the rate of change in the satellite orientation will be dependent on the Attitude Determination and Control System of the satellite.

4.2   Combined effects

Given that polarization control is needed for the duration of a satellite pass, which is on the order of minutes, the temperature-induced phase shift will primarily cause an absolute phase shift that will not change significantly over the course of a satellite pass, and will likely stay within a fraction of 2π. This phase shift must still be actively monitored ahead of a pass since it would vary from day to day.

The polarization drift due to fiber motion will induce a phase shift that will change over the course of a satellite pass, requiring active monitoring and compensation through the duration of a pass to ensure sufficient frame alignment to meet the QBER requirement. If a single phase control system is used to correct for phase shifts within the PM fiber and frame misalignment between the ground station and satellite, both effects will need to be combined using data from phase monitoring on the ground station and downlink beacon information from the satellite.

Chapter 5

Polarization control

Polarization control ensures frame alignment between the ground station photon source and the detectors on QEYSSat. Various polarization control methods are tested with polarization-maintaining (PM) fibers for their degree of polarization response, repeatability, and stability, to explore their suitability for polarization control.

The polarization control method would need to be automated, capable of providing continuous polarization control over the course of a satellite pass. It would need to continuously monitor the polarization state of the states leaving the ground station telescope through a polarization pick off, and then make necessary changes to the phase through an active control loop.

5.1 Polarization maintaining fibers

Polarization control is frequently performed in single mode (SM) fibers, and many commercial solutions exist for both free-space and in-line polarization control in SM fiber. Polarization control in polarization-maintaining (PM) fibers is typically performed by coupling light into one of the polarization-maintaining eigenmodes, whose phase is adjusted by modifying the optical path length within the PM fiber, such as by physically stretching the fiber using a piezoelectric tube [Nak+23]. However, this is insufficient for BB84, which encodes states in two orthogonal bases.

Free-space polarization control, such as by using waveplates in a free-space bridge, are common to both SM and PM fibers. One such free-space implementation was shown in an earlier airborne experiment [Pug+17] using an earlier prototype of the WCPS. In-line polarization control devices such as paddle controllers and fiber squeezers are commonly used for SM fibers, where mechanical stress is introduced to break the degeneracy of the polarization eigenmodes. The induced birefringences causes the fibers to behave similarly to a waveplate, which can be used to produce an adjustable phase shift [Col04]. This procedure is not as straightforward in PM fibers due to its large internal birefringence. Additionally, it is difficult to identify the orientation of the fast / slow axis of a PM fiber a segment of a jacketed PM fiber far away from a fiber endface.

5.2   In-line methods

An in-line control method involves tuning the polarization state of light while it is in a fiber. The fiber squeezer is one example, capable of tuning the polarization state of light by inducing birefringence, therefore introducing a phase shift along some axis related to the direction of the applied force. The three-paddle controller is capable of tuning polarization states to an arbitrary position on the Poincare sphere, in the case of single-mode fibers.

An in-line solution would be preferred for the WCPS and QOGS. Free-space solutions often require moving waveplates, which can cause intensity fluctuations, affecting the signal and decoy state intensities from the WCPS. The wedge present in waveplates can also create beam wander, affecting satellite pointing accuracy for the QOGS transceiver telescope.

Common methods of polarization control for single-mode fiber are investigated for their suitability to be adapted as polarization control for PM fiber.

5.2.1   Fiber squeezer

A simple method of adjusting the birefringence of a fiber is by applying a lateral force to it. When applied to single-mode (SM) fibers, it breaks the degeneracy between the two polarization eigenmodes due to the circular symmetry of the fiber, and the induced birefringence causes the SM fiber to behave like a variable

waveplate [SK81]. When applied to polarization-maintaining fibers, the existing birefringence is altered due to the change in the stress distribution across the fiber. Moreover, this change is dependent on the angle of the applied transverse force relative to the fast and slow axes of the PM fiber [NOS86].
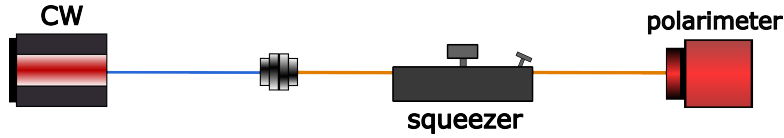
Figure 5.1: Single mode fiber-coupled light from a CW 780nm laser source is coupled into a PM fiber patch cable, passing through a Thorlabs CPC 900 in-line fiber optic polarization controller. The PM fiber output is coupled into a Thorlabs PAX1000IR1 polarimeter to measure the phase response.

A commercially available in-fiber squeezer was used for characterizating the squeezer response. The Thorlabs CPC 900 in-line fiber optic polarization controller was used on a 900µm jacket PM fiber patch cable passing through it. The fiber squeezer itself consists of thin, flat metal "tooth", which applies a varying force over approximately an inch in length as a pressure adjustment screw was turned. The metal "tooth" itself sits within a rotating section so that that the transverse pressure can be applied from any angle within somewhat less than a 90° angle.
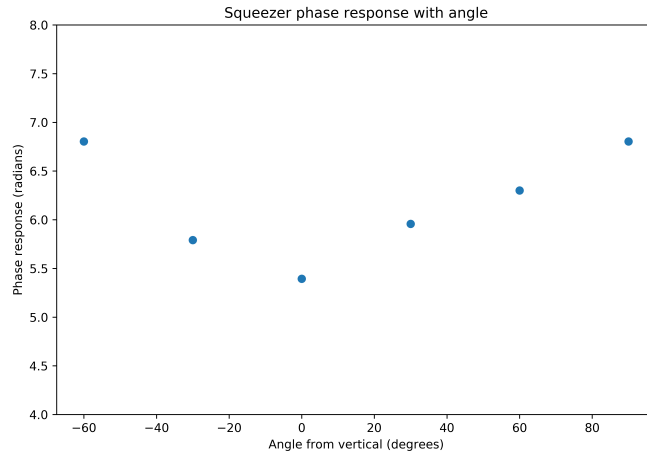
Figure 5.2: PM fiber fiber was inserted and held in the polarization controller by fiber holding clamps on the ends of the controller. The angle of the pressure adjustment knob was varied and measured by a protractor. Four turns were applied to the squeezer slowly by hand, and then allowed to rest for several seconds until the polarization state stabilized to a new state before being measured by the polarimeter. The angle of the applied force is defined with $0°$ being the vertical

The phase change induced by the polarization controller is seen to depend on the angle of the applied force, reaching a minimum near $0°$ and increasing for larger angles. However, the form of the relationship between the angle and the induced phase change on PM fiber is not clear. The exact relationship may be complex, depending on multiple other factors. For example, the pressure sensitivity of a single-mode fiber is dependent on the thickness of the Hytrel coating around it [Gia+82]. Additionally, accurate angular measurements were not possible since there are angle markings on the controller itself. The knob itself also does not allow for a direct force measurement to be made on the fiber. Additionally, there is no simple way to determine the orientation of the fast / slow axes in a jacket fiber patch cable, in a section far away from the ends of the patch cable. A careful characterization of PM fiber response to lateral stress would be best done by other methods.

5.2.2 Paddle controller

Another common method for polarization control in single-mode fiber is the 3-paddle controller. Fibers are wound about each of the paddles of the controller, secured in place, before the controller paddle angles are adjusted. The induced torsional forces break the degeneracy of the polarization eigenmodes, creating a phase shift that is dependent on the number of times that the fiber is wound about the paddle. A polarization controller can be made from a 3-paddle controller by selecting the approprimate number of fiber winds such that the 3-paddles approximately a QWP-HWP-QWP configuration [Col04].

For a PM fiber, the existing birefringence make the characterization more difficult, since the exact phase response will depend on the exact set of mechanical stresses induced on the PM fiber, as well as the orientation of the PM fiber inside the grooves of the controller. To try to isolate the effect of the rotating paddles on the PM fiber, a three-paddle controller was disassembled so that the central paddle could be motorized, while the two paddles on either side were held in place.
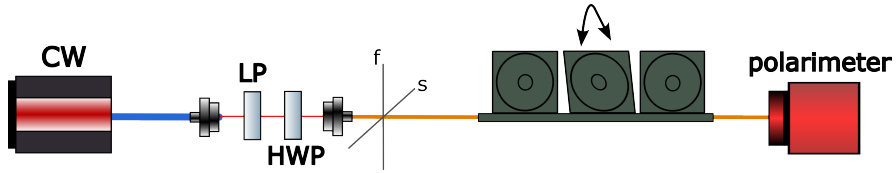
Figure 5.3: Light from a CW 780nm laser is coupled into free space. It is linearly polarized at the LP and then rotated into a $|D\rangle$ polarization with the HWP (where H/V are the s/f axes of the PM fiber. The central paddle was motorized with a rotation mount, and controlled with a Picomotor 8742 controller. Motion is programmed and executed by laptop software, and the phase response is measured by a Thorlabs PAX1000IR1 polarimeter.
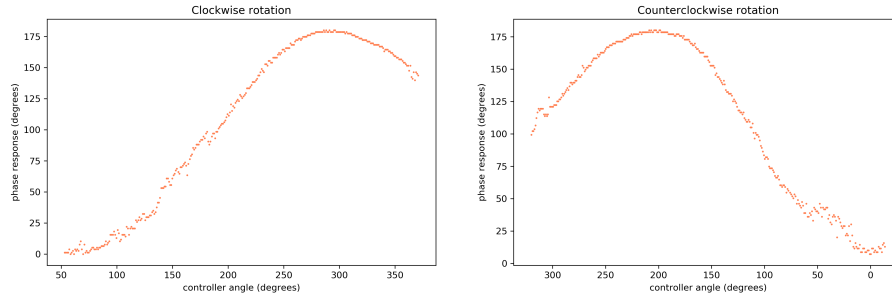
Figure 5.4: The paddle controller angle was adjusted slowly over 90 seconds using a Picomotor controller. The paddle moved in a continuous fashion at a constant speed in one direction. The fibers were allowed to relax for several seconds before being rotated in the opposite direction, at the same speed over the same amount of time.

For small angles, the phase response was clear and followed a sinusoid-like curve as a function of the controller angle. The phase response is seen to be nearly reproduced in reverse when the paddle controller was moved in the opposite direction, back to its starting position. Repeating the experiment for small motions in a single-direction at a fixed speed showed that this phase change is generally smooth and can be undone by moving in the opposing direction. However, there was not an obvious relationship between the turning points of the phase response and the paddle angle. The lack of knowledge about the precise orientation of the PM fiber throughout the grooves of the paddle also makes it difficult to create a model of the PM fiber in the paddle controller.

A paddle controller used for polarization control of PM fibers would also need to be able to move in more complex paths; the induced phase change by a PM fiber might change sign multiple times over a period of time. Thus, a more complicated test of the paddle controller's repeatability and robustness made.
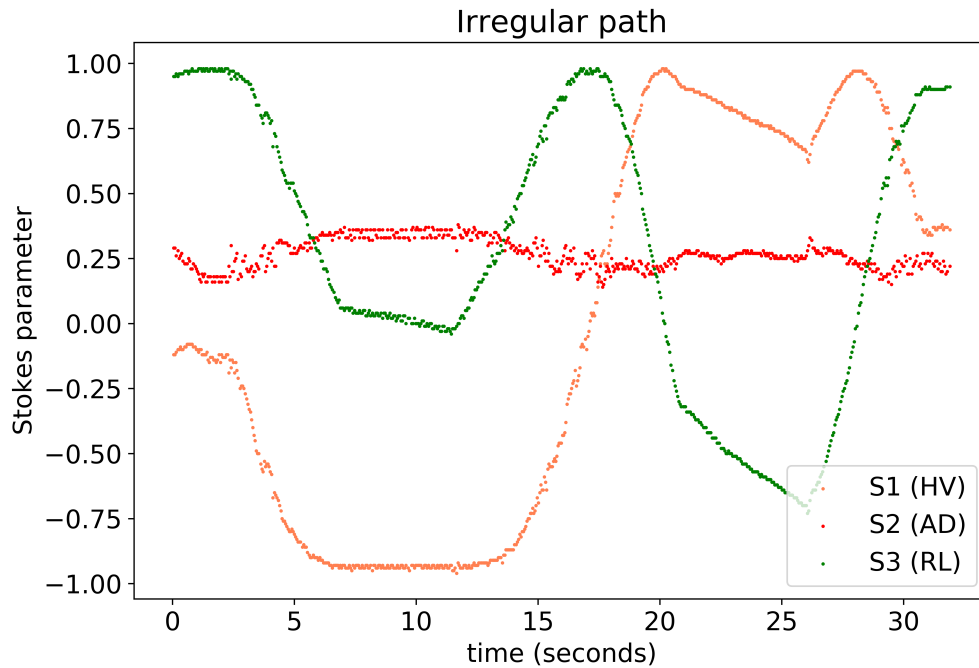
Figure 5.5: A more complex path was programmed, with two changes in direction and a larger angle rotation of up to 540 degrees. The polarization state motion became irregular and even sharply discontinuous at different places; each of the Stokes parameters of the polarization state are plotted as a function of time.

The phase response becomes irregular for the more complex path. At larger rotation angles, the phase changes become jagged and discontinuous. The discontinuous changes in the phase response suggest that some slippage may be happening within the fibers inside the paddle controller. The slippage and relative frictional forces between the fibers held in the groove are difficult to model and predict in practice.

The paddle controller is also limited by the fact that it cannot be turned too many times, since the PM fibers held within them would eventually snap. This limits the maximum phase response that can be implemented by a single paddle controller, though this problem may be mitigated by having multiple paddle controllers.

5.2.3 V-grooves

A more controllable way of applying tranverse stress to PM fibers is by using an unjacketed fiber seated in a v-groove. For shorter fibre lengths, the polarization axes orientation of the fiber can also be more readily controlled. The fiber can be allowed to hang freely from either connectorized end. Any twists in the fiber would induce a torsional force on the fiber, causing the fiber to rotate until the twists are undone. The polarization axis orientation should be consistent throughout the fiber; by aligning the polarization axis orientation at the ends of fiber ferrule endface, the polarization axis orientation throughout the length of the fiber would also be known.

A v-groove was machined from a piece of aluminum, creating notches with a depth of 100µm at a 90° angle. Bare, coated Thorlabs PM780-HP was allowed to be seated in the v-grooves. Since they have a coating diameter of 245µm [Tho05], they are seated partially in the v-groove, allowing lateral stress to be applied to it by placing a weight over it.
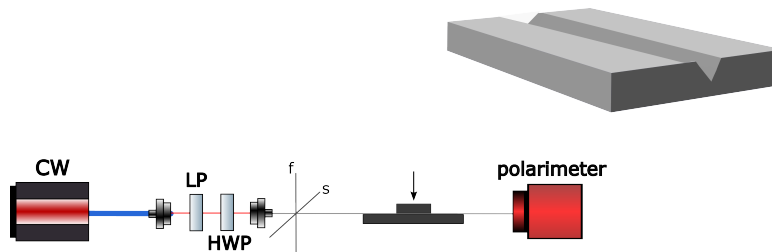
Figure 5.6: CW 780nm light was coupled into free space, set to a linear polarization (LP) and rotated to the $|D\rangle$ polarization before being coupled into bare PM fiber. The bare fiber was gently stretched taut and secured with tape near the ends of the v-groove. Force was applied by placing weights on a separate flat piece of metal, over a length of 60.3mm.

Weights were placed on the flat piece of metal, to investigate the phase response of the v-groove.
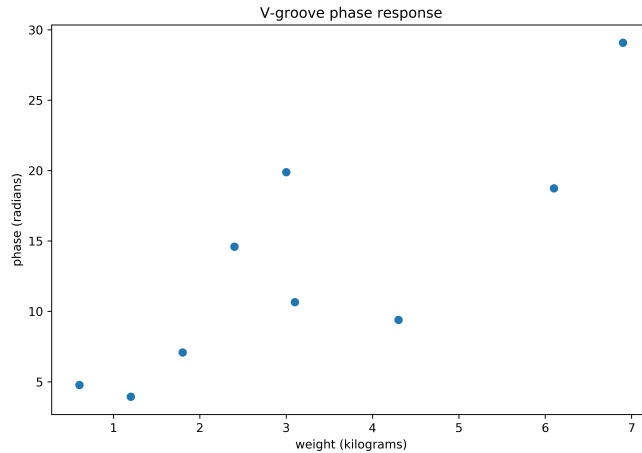
Figure 5.7: Weights were slowly placed onto the v-groove over the metal platform, and the phase response was extracted from a polarimeter monitoring the phase change.

There is a general trend in the phase response where the greater force from larger weights introduce a greater phase response. However, this relationship is rather irregular and this data alone does not clearly suggest a particular curve fit. A large contributing factor to the noise in the data is the fact that weights were lowered manually – this means that the weight is applied at uneven rates, creating uneven phase changes. In the ideal case, a smooth and even change in force should be applied, such as with an electromagnet or some other actuation system. The hysteresis of the phase response in a fiber makes this more important. A more careful characterization is necessary to understand the phase response with a v-groove squeezer.

Care was taken not to kink the bare fiber anywhere, particularly near the connectorized ends and at the v-groove. The fragility of this set up is a drawback to a potential v-groove solution. Future work can also investigate the possibility of using a v-groove to hold fibers with a 900µm jacketed patch cables, where the patch cables are kept relatively short so that there is a strong relation between the polarization axes at the fiber endfaces and the polarization axes throughout the patch cable.

An important factor to explore with the v-groove is the phase response as a function of the angle between the transversely applied force and the polarization axes

of the PM fiber. To better hold the fiber itself, differing v-groove depths should also be explored. The depth of the v-groove will also influence the angle formed between the fiber and the groove, which will also impact the phase response. The angle of the v-groove itself can also be varied. Other factors may also affect the phase response, such as the use of coated and uncoated fibers, and the frictional forces between the fiber and v-groove [KU81].

Another factor to consider in an implementation of polarization control is the mode-coupling within a PM fiber. Applying physical stresses on PM fiber can induce mode-coupling [THN88], changing the ratio of magnitudes of the fast / slow components. This change cannot be corrected for using only the phase adjustment from a PM fiber polarization controller. In addition, such a change might not be possible to correct using only the unitary operations of a waveplate, since the four polarization encoded states must be corrected simultaneously. Any implementation of polarization control based on lateral stress (or any physical stress) must be careful not to introduce significant mode-coupling.

5.3   Free-space methods

Polarization control is commonly performed in free space. Wave plates and polarizers make this straightforward process. In general, it is possible to transform an arbitrary polarization state into another polarization state using three waveplates [SM90]. They are also readily motorized, with widely available commercial solutions. However, the use of a free-space bridge reduces coupling efficiency, and introduces intensity fluctuations when moving optical components are used. A wedge present in optical components can also create beam wander, potentially causing substantial error for satellite pointing if the free-space polarization control is located within the transceiver telescope.

5.3.1   Liquid crystal retarder

The liquid crystal retarder (LCR) is another option of a free-space polarization controller. The liquid crystal retarder uses no moving parts and does not create beam wander. Moreover, it has a temperature dependence and care must be taken if it is to be used for phase control.
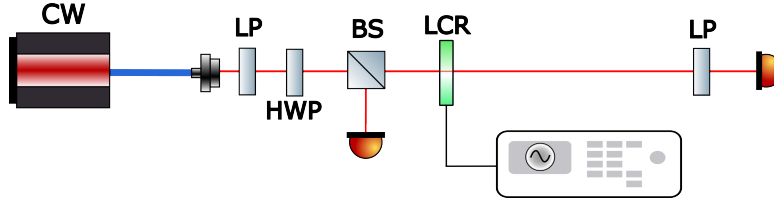
Figure 5.8: CW laser light at 780nm is coupled from single-mode fiber into free space, where a linear polarization (LP) eliminates any elliptical component in the laser light and a half-wave plate (HWP) to set a $|D\rangle$ polarization. A 50/50 beam splitter is used to monitor the power output of the laser, due to possible fluctuations of the laser light output. An LCR with its axes aligned to H/V is driven by a function generator. The LCR output passes through another LP set to $|D\rangle$ before being measured by a Thorlabs PM100A power meter.

The LCR is driven by a square wave from a function generator, while the square wave amplitude is varied. The LCR has a retardance decreasing with the driving amplitude, inducing a phase shift ϕ on the transmitted state. The input state will thus emerge somewhere on the DRAL circle as the state

$$|\phi\rangle = |H\rangle + e^{i\phi}|V\rangle, \tag{5.3.1}$$

where $\phi = 0 (\mathrm{mod}\, 2\pi)$ is the original state input state.

The intensity fluctuations from the CW laser light make it necessary to normalize the power meter readings as a fraction of the power received by the monitor. The ratio of the transmitted intensity to the monitor arm intensity will be the measure of the phase, where the ratio is maximized for a $|D\rangle$ output state and minimized for a $|A\rangle$ output state.
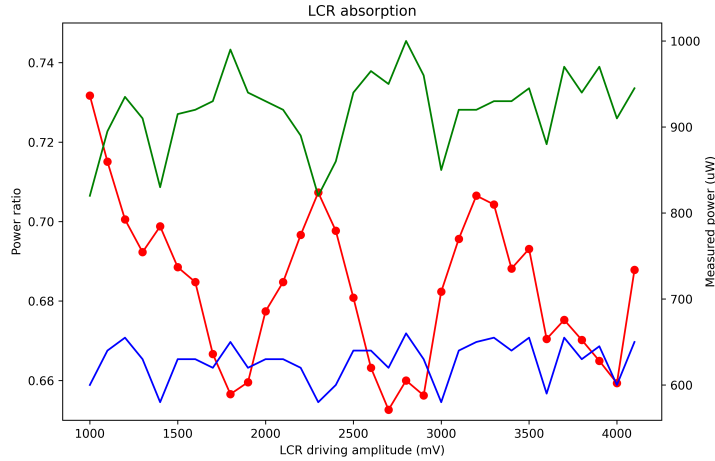
Figure 5.9: The monitor arm intensity (blue) and transmitted intensity (green) from the LCR, with the ratio of their intensities $I_{\mathrm{transmit}}/I_{\mathrm{monitor}}$ (red) indicating the LCR induced phase. The LCR driving amplitude was taken from 1000mV to 4100mV in increments of 100mV.

The LCR shows a periodic response, with each period indicating a π phase shift. The irregularly spaced minima at 1.8mV, 2.7mV, and 4.0mV show that this phase response is not linear with the change in driving amplitude. Notably, the transmitted state is never extinguished, suggesting that the transmitted state was not fully rotated to the orthogonal $|A\rangle$ polarization. The diminishing amplitude of the oscillations also suggest an absorption that is varying with the driving amplitude of the oscillator. Since this implies that the LCR will have varying transmissivity for different phase shifts, it would not be suitable for polarization control due to the intensity fluctuations it would introduce.

The temperature dependence of an LCR must also be considered if it is to be used for polarization control. This may be mitigated by placing it in a temperature controlled environment in the lab and carefully characterizing the LCR, or designing a temperature-stable module using multiple LCR's [Reh+22; Reh+23].

5.3.2 Turning a waveplate

A waveplate is a piece of birefringent material (or two pieces of birefringent material sandwiched together). Therefore, it will induce a phase shift proportional to

the optical path length taken by the fast and slow components of light propagating through it. One way of inducing a phase shift is thus to turn the waveplate along an axis *parallel* to the flat face of the waveplate. In this thesis, the use of the waveplate in this fashion will be referred to as "turning" a waveplate, while the "usual" method of rotating a waveplate along an axis perpendicular to its flat face will be referred to as "rotating" a waveplate.

The beam emerging from the waveplate will continue to travel in the same direction with the same $\vec{k}$-vector, but it will be displaced due to the slanted path it traversed in the waveplate.

The waveplates used are zero-order waveplates, which are typically composed of two pieces of birefringent quartz sandwiched together, with its fast and slow axes flipped relative to the other. Each piece alone induces a phase shift that are many multiples of π, but their thicknesses are chosen such that the net phase shift is (close to) exactly $\pi/2$ for normally incident light. In reference with literature, an analytic model was made to compute the phase shift induced by turning a waveplate, considering the o- and e-rays travel through the two pieces of quartz separately. The o- and e-rays of an incoming beam separate at the waveplate air-quartz interface, for non-normal angles of incidence [BW80; HD88; Zhu94].
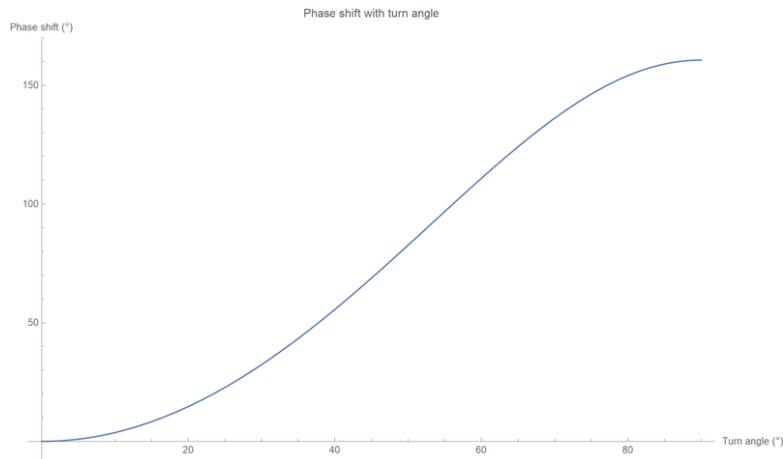
Figure 5.10: The phase shift induced by a single waveplate, as a function of the turn angle.

An experimental set up was built with two waveplates of the same part number mounted on rotating stages. In order to compensate for the beam deviation from

a single turning waveplate, a second waveplate can be turned by the same amount in the opposing direction. This would also have the effect of doubling the phase shift compared with a single waveplate. The phase shift induced by a single waveplate was first examined. The measured intensities from the PBS outputs were combined to calculate the phase shift.
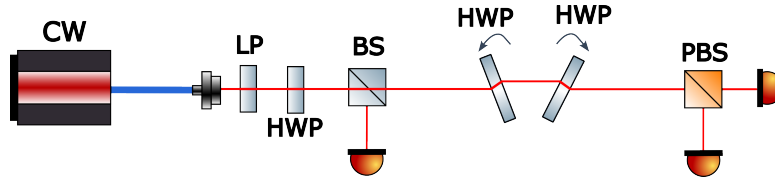
Figure 5.11: The fiber-coupled output from a CW 780nm laser is taken to free-space and set to $|D\rangle$ by a linear polarization (LP), before being split at a 50/50 beam splitter (BS) where the reflected arm is measured by a power meter as an intensity monitor for laser intensity fluctuation. The transmitted beam passes through two 808nm zero-order half waveplates of the same part number mounted on a manual rotation stage, either of which may be turned, where both waveplate axes are aligned to H/V. The transmitted waveplate output is then split off at a polarizing beam splitter (PBS) to be measured by two power meters in the D/A basis.

The zero-order waveplate is seen to have a somewhat angle-insensitive phase response for very small angles, though the phase response from further turning becomes much greater at angles past approximately 10°. In practice, it will not be possible to turn the waveplate much further than 30°, since the beam will begin to clip the mount holding the waveplate.
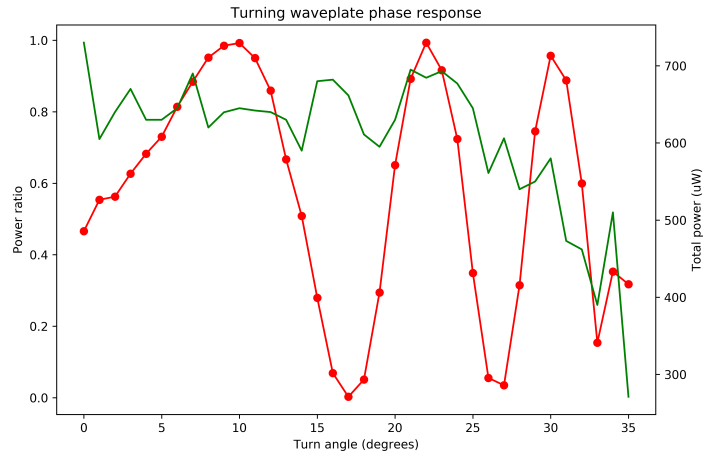
Figure 5.12: Intensity variation from turning a single waveplate in 1°
increments until the beam began to be clipped, the curve plotted is
the ratio of the power between the two detectors at the PBS output
(red). The total power measured (green) is also plotted to indicate
when the beam begins to be clipped.

The measured data shows a phase shift that begins gradually until a turn angle
near 10°, before the phase shift becomes faster with larger turn angles. The results
here agree with the theoretical model. The minima of the phase response is also
near 0, which implies that the optical element was indeed taking state attained
at the maxima to its orthogonal state, in contrast with the tested LCR.
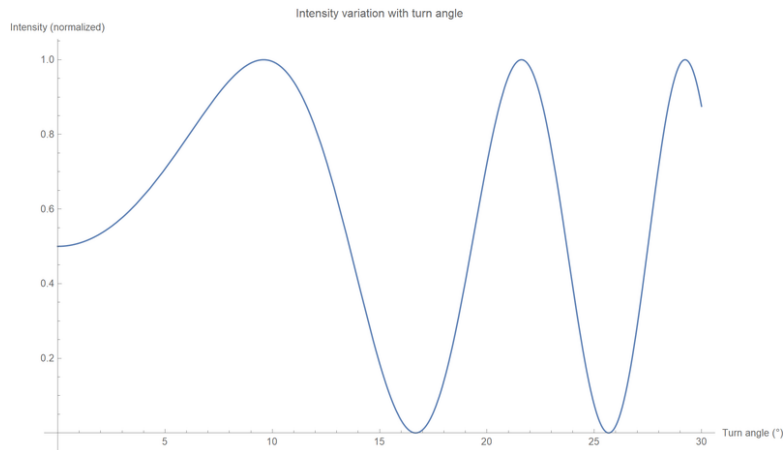
Figure 5.13: Theoretical model of the intensity variation expected
from the experiment in Figure (5.11), due to the phase shift induced
by turning a zero-order waveplate.

65

The beam deviation formed by turning a waveplate was also investigated. As a waveplate is turned, it would deviate a transmitted beam further. Since the core of a single-mode fiber is only several microns in radius, this may be sufficient to substantially impact the coupling efficiency back into PM fiber. This would create intensity fluctuations dependent on the phase adjustment.
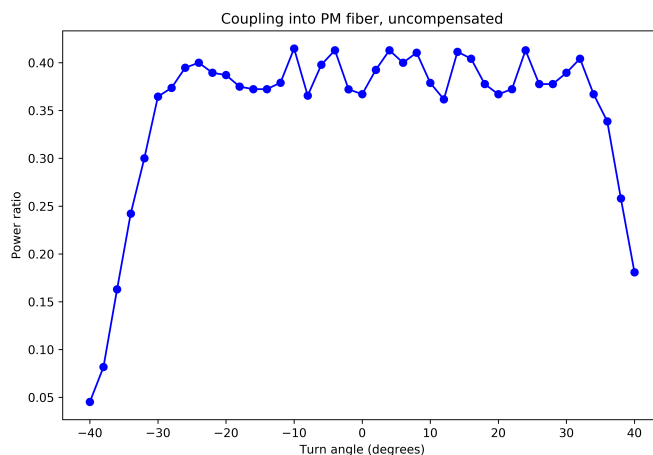
Figure 5.14: The first waveplate of Figure (5.11) is turned in either direction in 1° increments so that beam deviated is uncompensated. The coupling is measured as a ratio of the measured power coupled back into fiber and the power measured by the intensity monitor.

The coupling is seen to be roughly constant, if somewhat irregular, before it sharply drops off as the beam is clipped by the edges of the mount.

The same measurement was repeated with both waveplates turning in opposite directions, to compensate for beam deviation.
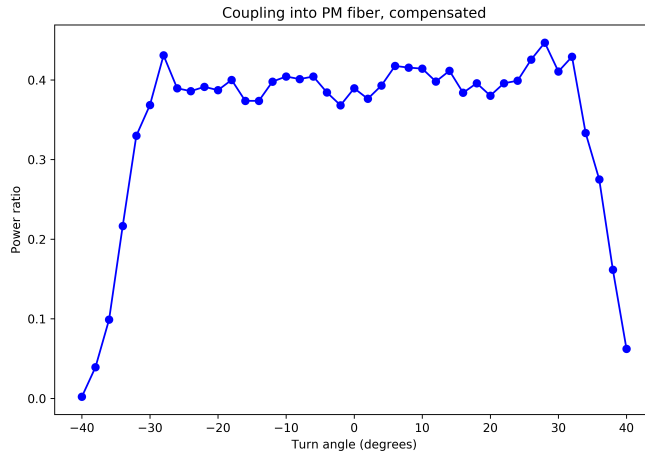
Figure 5.15: Both waveplates of Figure (5.11) are turned in opposing directions to compensate for beam deviation. The angles are measured relative to the first waveplate as in Figure (5.14).

The overall coupling is also roughly constant, though they appear to fluctuate less with changing angles. A clear difference between the uncompensated and compensated waveplates is not seen. The coupling drops off near the same angles as the beam becomes clipped by the mount.

To accurately determine the performance of a turning waveplate, measurements with better precision should be carried out. A motorized rotation stage can be used to scan across a range of angles, since the repeated increments of the rotation stage position will cause backlash that can affect measurements precision.

If this method were to be used for polarization control, the position of the waveplates should be kept in a region where it is sensitive to phase changes in either turn direction (ex. around 20°) prior to a satellite pass where active control will be needed. The position should also be kept at an angle that is not too close to the end of the turning range of the waveplates, to ensure sufficient "runway" in either direction of phase change. Two waveplates should also be used, not only for beam deviation compensation, but also to increase the total phase shift that is induced. Nevertheless, this method will only provide a "runway" of no more than several πrad, meaning that it can only be used in cases where smaller phase adjustments will suffice.

5.3.3 Rotating waveplate

Wave plates allow for arbitrary polarization rotations to be performed. However, waveplates typically have some wedge on them, causing unwanted beam steering to transmitted beams as the waveplates are rotated. This can cause a large beam wander over long distances, such as in a satellite link, or coupling issues, such as in a free-space bridge between single-mode fibers.

The impact of a rotating waveplate on coupling was investigated, since intensity variations must be minimized in any potential polarization control system.
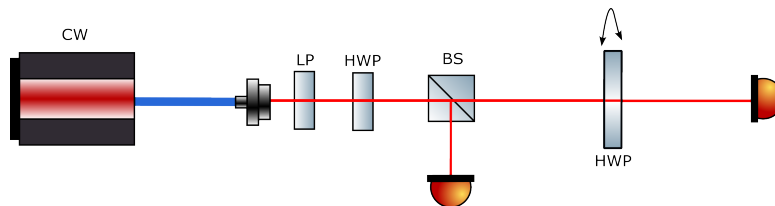
Figure 5.16: A 780nm CW laser source was coupled into free-space and set to a linear polarization by the linear polarization (LP). A beam splitter (BS) picks off part of the beam to an intensity monitor. A waveplate on a rotation mount is rotated before the beam is coupled back into single mode (SM) fiber and measured at a power meter.
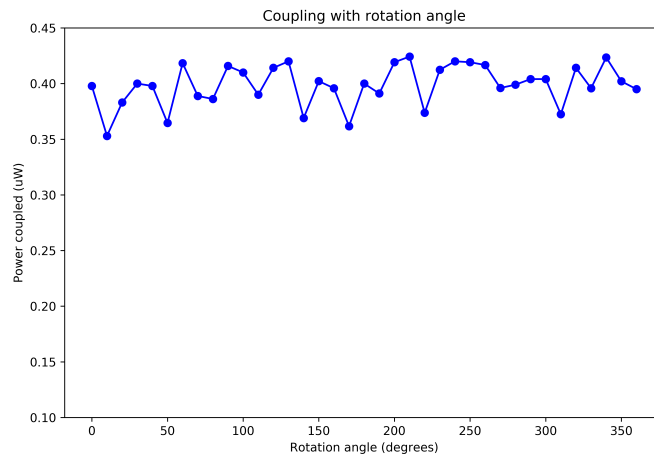
Figure 5.17: The coupling is plotted as a ratio of the intensities at the laser power monitor and the free space monitor, due to laser power fluctuations. Measurements were taken in 5° steps across the entire rotation.

There is not a definitive trend in the impact to the coupling, though the coupling ratio may possible be smaller around the $0° - 50°$ region and higher around the $200° - 250°$. It is noted that the errors in both detector measured would are combined in the ratio plotted above. A more careful measurement with more stable laser power would help with the characterization of the impact of waveplate wedge to coupling efficiency. A measurement using a motorized mount moving in a continuous motion will also help. The waveplate was rotated by free hand, which may have also moved the waveplate slightly, causing the irregular coupling seem in the data above between adjacent data points.

5.4   Comparison of methods

The various methods of polarization control above are compared below.

In-line	Advantages / Disadvantages
Squeezer	(Advantage) Simple device
	(Disadvantage) Hysteresis in phase adjustment
Paddle controller	(Advantage) Smooth, repeatable motion for small angles
	(Disadvantage) Unpredictable for irregular motions
V-groove	(Advantage) Readily machined in-house
	(Disadvantage) Works on bare fiber which are fragile

Free-space	Advantages / Disadvantages
LCR	(Advantage) Easily controlled with no moving parts
	(Disadvantage) Retardance dependent absorption
Turning a waveplate	(Advantage) Well-defined phase shift with no hysteresis
	(Disadvantage) Limited phase change in either direction
Rotating a waveplate	(Advantage) Unlimited phase correction in either direction
	(Advantage) Easily motorized
	(Disadvantage) Potential beam steering

Of the options explored, the best in-line solution appears to be one that relies on applying lateral stress to the fiber, while the rotating waveplate appears to be the favored free-space solution.

In the case of an in-line solution, applying lateral stress seems to be best due to

the relative predictability of the phase response. While the hysteresis and physical factors prevent an exact phase response from being predicted, a control system can still be built from an in-line solution. A v-groove or squeezer system may both work. A solution using jacketed fibers may be better due to the fragility of bare fiber, squeezing the fibers with actuators whose direction of applied force may be varied to maximize the phase response.

In the case of a free-space solution, the rotating waveplate seems to be better, as long as the intensity fluctuations can be kept minimal. The rotating waveplate can be added to the existing free-space bridge within the weak coherent pulse source (WCPS), making a solution easy to implement. Since the waveplate is on a rotation mount, it may apply unlimited phase adjustments in either direction, something that cannot be done with any of the in-line methods or the turning waveplate solution. This solution may also be more easily adapted to other quantum sources that also require polarization control, such as an entangled pair source.

5.5   Polarization control system

A polarization control system for the WCPS will require a polarization pick off to monitor the total phase drift that has accumulate throughout the fiber links to the transceiver telescope of the Quantum Optical Ground Station (QOGS). This pick off needs to be placed at the aperture of the transceiver telescope.

The polarization control system itself can be placed anywhere along the PM fibers and free-space bridges of the WCPS and QOGS. A benefit of using PM fiber is that the polarization rotations constrained to a circle commute, whereas arbitrary polarization rotations induced by a SM fiber do not. It can be incorporated into the acquisition, pointing, and tracking (APT) system of the transmitter telescope as it was in the airborne experiment [Pug+17], although a different location would avoid beam steering errors that can become unacceptably large for a satellite link.

An in-fiber polarization control solution for PM fiber can be placed on a suitable fiber. This is a 900µm fiber for a fiber squeezer solution, and a bare fiber for a v-groove solution. Both are relatively fragile compared with a typical 3mm jacket; such an in-fiber polarization control solution is best incorporated into the WCPS

itself.

A free-space polarization solution is most easily incorporated into the free-space bridge in the WCPS, at the entrance of the phase modulator assembly. The linear polarization (LP) currently setting states to a $|D\rangle$ polarization can be motorized to apply the phase adjustment, and a fixed QWP can be added to rotate the adjusted linear polarization state to the DRAL circle. The state $|\phi\rangle = |H\rangle + e^{i\phi} |V\rangle$ entering the PM fiber would be the state required for frame alignment between the states at the sender and the measurements on QEYSSat. Given the simple implementation, this is likely the best option for polarization control, as long as the intensity fluctuations can be kept acceptably low.
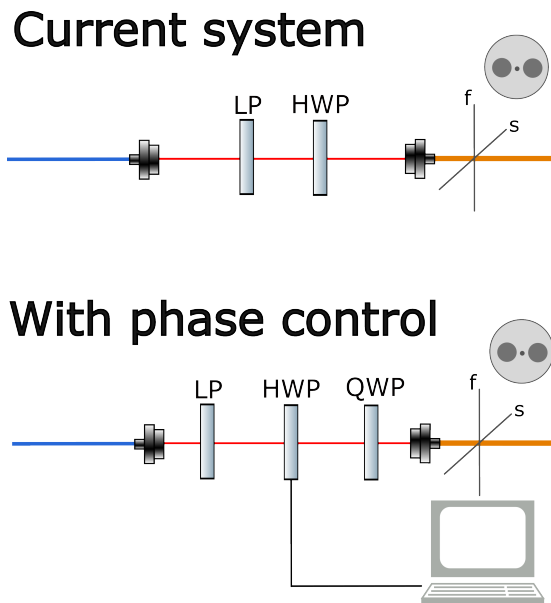
Figure 5.18: The current WCPS free-space bridge uses a linear polarizer to remove any circular components of the laser light polarization, followed by a half-wave plate (HWP) to set a $|D\rangle$ polarization (where H/V are the slow/fast axes of the PM fiber). One method of phase control is to motorize the existing HWP and add a QWP. The HWP would rotate the linear polarized states within the plane of linear polarizations, while the fixed QWP will take the states to the DRAL circle.

A standalone free-space bridge in contrast would require three waveplates - a fixed QWP to rotate states from the DRAL circle to the linear polarization, a motorized HWP to apply the appropriate phase correction, and another fixed QWP to rotate

the corrected linear polarizations back to the DRAL circle.

To determine the required phase corrections, the phase drift within the WCPS and QOGS will be needed, as well as the satellite orientation. The phase drift on the ground systems will be determined by the polarization pick-off at the telescope apaerture, while the satellite orientation is communicated by a linearly polarized downlink beacon from the satellite. A separate downlink beacon measurement will be necessary for this. A completed polarization control system would comprise of a polarization pick off, polarization control mechanism, both integrated with the WCPS.
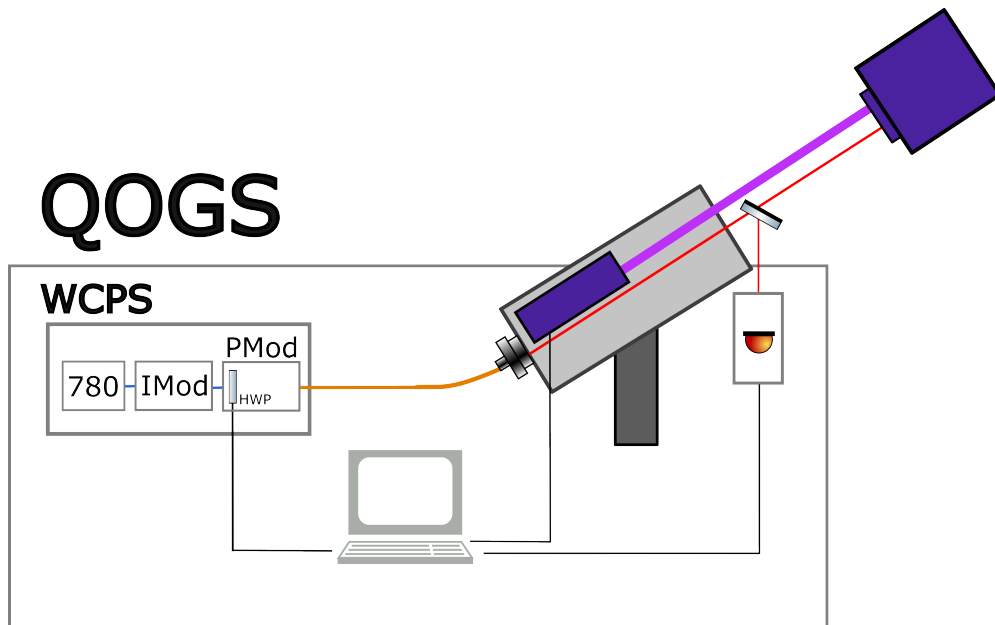
Figure 5.19: The high level diagram of the polarization control system with phase drift information from a polarization pick off located at the tranceiver telescope aperture and satellite orientation from a downlink beacon polarization measurement. The polarization pick off collects a small portion of the quantum uplink (red) while the beacon measurement collects a portion of linearly polarized classical downlink (purple). Electrical cables are denoted with black lines; the computer processor and detectors for the pick-off and downlink beacon are only indicative – measurements at multiple settings will be needed to obtain sufficient phase information. The necessary phase adjustment can be implemented by a motorized half-waveplate in the phase modulation assembly of the weak coherent pulse source (WCPS).

The polarization pick off in Figure 5.19 above will only collect a very small portion of the quantum uplink signal, away from the center of the Gaussian beam. Only several hundred photons are needed to determine a polarization state needed for frame alignment [HBJ20]. For the WCPS quantum source, this corresponds to a square mirror only a few millimeters across, although a larger mirror will be practical. Since many of the weak coherent pulses will contain no photons and only a small portion of them will be collected by the pick off, timing analysis will be needed to match detections with the pulses that were encoded by the WCPS. The downlink beacon measurement will need to measure the linear polarization of the classical downlink beacon. One option is a separate telescope (as indicated in Figure 5.19). Given the beam divergence of the downlink beacon, the expected signal will be relatively weak, in the nanowatts regime. However, this would still be a classical signal. A computer in the Quantum Optical Ground Station (QOGS) will compute the necessary phase adjustment for the WCPS, considering the phase drift accumulated in the PM fibers of the ground station and the QEYSSat satellite orientation, in order to ensure frame alignment between the ground station and satellite. This phase adjustment can be performed in a number of ways, including by using a half-waveplate in the free-space bridge of the weak coherent pulse source (WCPS).

Chapter 6

Conclusion

This thesis described work on a weak coherent pulse source (WCPS) prototype to be used in a satellite uplink for the QEYSSat mission. A wave packet model was described in chapter 2 to better understand the tolerances on fiber lengths mismatches and angular misalignment. The key factors contributing to phase drift in PM fiber were examined in chapter 3. Various methods of polarization control in polarization-fiber were explored in chapter 4.

The wave packet model in chapter 2 showed that given the relatively long pulses from the weak coherent pulse source (WCPS) compared with the accumulated differential group delay in the weak coherent pulse source (WCPS) and Quantum Optical Ground Station (QOGS), fiber length matching is not a critical issue for the weak coherent pulse source (WCPS). However, angular alignment is a critical component that must be performed carefully to minimize the QBER of the pulses produced by the weak coherent pulse source (WCPS).

The phase drift characterization in chapter 3 showed that the overall phase shift expected over the course of the entire satellite pass will be less than 2πrad. Active polarization control will be needed, but the polarization control system will not require a very large range of phase shift. Moreover, phase drift will appear over the course of the day, requiring a polarization control system to apply corrective phase adjustments prior to each satellite pass.

PM fibers for future WCPS can be prepared based on the tolerances computed from the wave packet model. The wave packet model may also be extended to

include multiple fiber joints and other aspects of the WCPS, or used to model fiber requirements on other quantum sources using PM fiber. The work on examining different methods of polarization control will also inform the design of a polarization control system for the WCPS.

Future work will involve implementing a polarization control mechanism, polarization pick off, downlink beacon polarization measurement, and integrating it with the WCPS, as described in section 5.5. A polarization control mechanism integrated into the free-space bridge of the WCPS is a simple option, while an in-line actuator system applying lateral force to fibers can also be installed within the WCPS. As part of a complete active feedback system, this system would need to be integrated with a polarization pick-off monitoring the polarization of states generated on the ground, and a downlink beacon polarization measurement monitoring the orientation of the satellite for frame alignment.

The polarization control system based on the work in this thesis will form part of the WCPS quantum source as part of the QEYSSat science demonstration, towards secure quantum communication across Canada.

Bibliography

[Ala+19]   Gorjan Alagic et al. *Status Report on the First Round of the NIST Post-Quantum Cryptography Standardization Process*. Tech. rep. NIST IR 8240. Gaithersburg, MD: National Institute of Standards and Technology, Jan. 2019, NIST IR 8240. DOI: `10.6028/NIST.IR.8240`. (Visited on 03/30/2023).

[And06]   Larry C. Andrews. *Laser beam propagation through random media*. SPIE Press, 2006, p. 782. ISBN: 9780819459480.

[Aws+22]   David Awschalom et al. *A Roadmap for Quantum Interconnects*. Tech. rep. ANL-22/83, 1900586, 179439. July 2022, ANL–22/83, 1900586, 179439. (Visited on 12/22/2022).

[BB14]   Charles H. Bennett and Gilles Brassard. "Quantum Cryptography: Public Key Distribution and Coin Tossing". In: *Theoretical Computer Science* 560 (Dec. 2014), pp. 7–11. ISSN: 03043975. DOI: `10.1016/j.tcs.2014.05.025`. (Visited on 01/21/2021).

[BL17]   Daniel J. Bernstein and Tanja Lange. "Post-Quantum Cryptography". In: *Nature* 549.7671 (Sept. 2017), pp. 188–194. ISSN: 1476-4687. DOI: `10.1038/nature23461`. (Visited on 03/30/2023).

[Bou+13]   J-P Bourgoin et al. "A Comprehensive Design and Performance Analysis of Low Earth Orbit Satellite Quantum Communication". In: *New Journal of Physics* 15.2 (Feb. 2013), p. 023006. ISSN: 1367-2630. DOI: `10.1088/1367-2630/15/2/023006`. (Visited on 01/23/2020).

[Boy07]   Robert W. Boyd. *Nonlinear optics*. Third. Academic Press, 2007. ISBN: 9780123694706.

[Buc04]   John A. Buck. *Fundamentals of optical fibers*. Second. John Wiley & Sons, 2004, p. 332. ISBN: 9780471221913.

[Bv05]   Samuel L Braunstein and Peter van Loock. "Quantum Information
           with Continuous Variables". In: *Quantum information with continu-
           ous variables* 77.2 (2005), p. 65.

[BW80]   Max Born and Emil Wolf. *Principles of optics. electromagnetic theory
           of propagation, interference and diffraction of light.* Sixth. Pergamon
           Press, 1980, p. 808. ISBN: 0080264816.

[Can23]   Government of Canada. *Quantum encryption and science satellite.*
           Feb. 2023. URL: https://www.asc-csa.gc.ca/eng/satellites/
           qeyssat.asp.

[Col04]   Edward Collett. *Polarized light in fiber optics.* SPIE, 2004. ISBN:
           9780819457615.

[Gia+82]   T.G. Giallorenzi et al. "Optical Fiber Sensor Technology". In: *IEEE
           Transactions on Microwave Theory and Techniques* 30.4 (Apr. 1982),
           pp. 472–511. ISSN: 1557-9670. DOI: 10.1109/TMTT.1982.1131089.

[Gis+02]   Nicolas Gisin et al. "Quantum Cryptography". In: *Reviews of Modern
           Physics* 74.1 (Mar. 2002), pp. 145–195. ISSN: 0034-6861, 1539-0756.
           DOI: 10.1103/RevModPhys.74.145. (Visited on 01/12/2021).

[GK04]   Christopher Gerry and Peter Knight. *Introductory Quantum Optics.*
           Cambridge University Press, 2004, p. 332. ISBN: 978-0521527354.

[Gla06]   Roy J. Glauber. *Quantum theory of optical coherence. Selected Papers
           and Lectures.* Wiley-VCH, 2006, p. 656. ISBN: 9783527406876.

[God+22]   Paul J. Godin et al. "Birefringence Compensation from Polariza-
           tion Maintaining Fiber Pairs". In: *Conference on Lasers and Electro-
           Optics.* Optica Publishing Group, 2022, AM2D.6. DOI: 10.1364/
           CLEO_AT.2022.AM2D.6. URL: https://opg.optica.org/abstract.
           cfm?URI=CLEO_AT-2022-AM2D.6.

[Grü+20]   Fadri Grünenfelder et al. "Performance and Security of 5 GHz Repe-
           tition Rate Polarization-Based Quantum Key Distribution". In: *Ap-
           plied Physics Letters* 117.14 (Oct. 2020), p. 144003. ISSN: 0003-6951,
           1077-3118. DOI: 10.1063/5.0021468. (Visited on 11/18/2022).

[HBJ20]   Brendon L. Higgins, Jean-Philippe Bourgoin, and Thomas Jennewein. "Numeric Estimation of Resource Requirements for a Practical Polarization-Frame Alignment Scheme for QKD". In: *Advanced Optical Technologies* 9.5 (Nov. 2020), pp. 253–261. ISSN: 2192-8584, 2192-8576. DOI: `10.1515/aot-2020-0016`. (Visited on 05/29/2021).

[HD88]   P. D. Hale and G. W. Day. "Stability of Birefringent Linear Retarders (Waveplates)". In: *Applied Optics* 27.24 (Dec. 1988), p. 5146. ISSN: 0003-6935, 1539-4522. DOI: `10.1364/AO.27.005146`. (Visited on 08/05/2022).

[Hec17]   Eugene Hecht. *Optics*. Fifth. Pearson, 2017. ISBN: 9780133977226.

[Hec93]   Jeff Hecht. *Understanding fiber optics*. H.W. Sams, 1993, p. 477. ISBN: 9780672303500.

[Hwa03]   Won-Young Hwang. "Quantum Key Distribution with High Loss: Toward Global Secure Communication". In: *Physical Review Letters* 91.5 (Aug. 2003), p. 057901. ISSN: 0031-9007, 1079-7114. DOI: `10.1103/physrevlett.91.057901`. (Visited on 01/12/2022).

[Iiz02]   Keigo Iizuka. *Elements of photonics*. First. Vol. 1. Wiley-Interscience, 2002, p. 1197. ISBN: 978-0471839385.

[ILM07]   Hitoshi Inamori, Norbert Lütkenhaus, and Dominic Mayers. "Unconditional Security of Practical Quantum Key Distribution". In: *The European Physical Journal D* 41.3 (Mar. 2007), pp. 599–627. ISSN: 1434-6060, 1434-6079. DOI: `10.1140/epjd/e2007-00010-4`. arXiv: `quant-ph/0107017`. (Visited on 05/23/2023).

[Jen+14]   T. Jennewein et al. "QEYSSAT a Mission Proposal for a Quantum Receiver in Space". In: *SPIE OPTO*. Ed. by Zameer U. Hasan et al. San Francisco, California, United States, Feb. 2014, 89970A. DOI: `10.1117/12.2041693`. (Visited on 02/23/2021).

[Kam81]   I. Kaminow. "Polarization in Optical Fibers". In: *IEEE Journal of Quantum Electronics* 17.1 (Jan. 1981), pp. 15–22. ISSN: 0018-9197. DOI: `10.1109/JQE.1981.1070626`. (Visited on 03/09/2021).

[KL10]   Pieter Kok and Brendon W. Lovett. *Introduction to optical quantum information processing*. Cambridge University Press, 2010, p. 488. ISBN: 9780521519144.

[KTO14]   Toshiya Kobayashi, Akihisa Tomita, and Atsushi Okamoto. "Evaluation of the Phase Randomness of a Light Source in Quantum-Key-Distribution Systems with an Attenuated Laser". In: *Physical Review A* 90.3 (Sept. 2014), p. 032320. ISSN: 1050-2947, 1094-1622. DOI: `10.1103/PhysRevA.90.032320`. (Visited on 12/14/2022).

[KU81]   A. Kumar and R. Ulrich. "Birefringence of Optical Fiber Pressed into a V Groove". In: *Optics Letters* 6.12 (Dec. 1981), p. 644. ISSN: 0146-9592, 1539-4794. DOI: `10.1364/OL.6.000644`. (Visited on 05/01/2021).

[Kys+17]   Martin Kyselak et al. "Phase Response of Polarization-Maintaining Optical Fiber to Temperature Changes". In: *Optica Applicata* (2017). DOI: `10.5277/OA170412`. (Visited on 04/30/2021).

[Li+09]   Yan-jie Li et al. "An Accurate Method for Alignment of Polarization-Maintaining Fiber with CCD Micro-Imaging System". In: *International Symposium on Photoelectronic Detection and Imaging 2009*. Ed. by Kun Zhang et al. Beijing, China, July 2009, 73841R. DOI: `10.1117/12.835670`. (Visited on 01/24/2023).

[LMC05]   Hoi-Kwong Lo, Xiongfeng Ma, and Kai Chen. "Decoy State Quantum Key Distribution". In: *Physical Review Letters* 94.23 (June 2005), p. 230504. ISSN: 0031-9007, 1079-7114. DOI: `10.1103/PhysRevLett.94.230504`. (Visited on 01/12/2021).

[Lou00]   Rodney Loudon. *The quantum theory of light*. Third. Oxford University Press, 2000, p. 438. ISBN: 978-0198501763.

[LP07]   Hoi-Kwong Lo and John Preskill. "Security of Quantum Key Distribution Using Weak Coherent States with Nonrandom Phases". In: *arXiv:quant-ph/0610203* (Jan. 2007). arXiv: `quant-ph/0610203`. (Visited on 01/19/2022).

[Mig+13]   Alan Migdall et al. *Single-photon generation and detection. Physics and Applications*. Elsevier Science & Technology Books, 2013, p. 616. ISBN: 9780123876959.

[Mun+15]   William J. Munro et al. "Inside Quantum Repeaters". In: *IEEE Journal of Selected Topics in Quantum Electronics* 21.3 (May 2015), pp. 78–90. ISSN: 1558-4542. DOI: `10.1109/JSTQE.2015.2392076`.

[Nak+23]   Tomohiro Nakamura et al. "Low-Loss Polarization Control in Fiber
            Systems for Quantum Computation". In: *Optics Express* 31.12 (June
            2023), pp. 19236–19254. ISSN: 1094-4087. DOI: `10.1364/OE.489082`.
            (Visited on 05/24/2023).

[NOS86]   J. Noda, K. Okamoto, and Y. Sasaki. "Polarization-Maintaining Fibers
            and Their Applications". In: *Journal of Lightwave Technology* 4.8
            (1986), pp. 1071–1089. ISSN: 0733-8724. DOI: `10.1109/JLT.1986.`
            `1074847`. (Visited on 03/09/2021).

[Pen+06]   Denis Penninckx et al. "Signal Propagation Over Polarization-Maintaining
            Fibers: Problem and Solutions". In: *Journal of Lightwave Technology*
            24.11 (Nov. 2006), pp. 4197–4207. ISSN: 1558-2213. DOI: `10.1109/`
            `JLT.2006.884189`.

[Pir+20]   S. Pirandola et al. "Advances in Quantum Cryptography". In: *Advances in Optics and Photonics* 12.4 (Dec. 2020), p. 1012. ISSN: 1943-
            8206. DOI: `10.1364/AOP.361502`. (Visited on 02/02/2021).

[PLA03]   Martin Pfennigbauer, Walter R Leeb, and Markus Aspelmeyer. "Free-
            Space Optical Quantum Key Distribution Using Intersatellite Links".
            In: (2003).

[Pug+17]   Christopher J Pugh et al. "Airborne Demonstration of a Quantum
            Key Distribution Receiver Payload". In: *Quantum Science and Technology* 2.2 (June 2017), p. 024009. ISSN: 2058-9565. DOI: `10.1088/`
            `2058-9565/aa701f`. (Visited on 04/23/2021).

[Ras83]   S. Rashleigh. "Origins and Control of Polarization Effects in Single-
            Mode Fibers". In: *Journal of Lightwave Technology* 1.2 (1983), pp. 312–
            331. ISSN: 0733-8724. DOI: `10.1109/JLT.1983.1072121`. (Visited on
            03/09/2021).

[Reh+22]   Jean Rehbinder et al. "Liquid-Crystal Based Drift-Free Polarization
            Modulators: Part I. Design and Operation". In: *Optics Express* 30.9
            (Apr. 2022), pp. 14966–14977. ISSN: 1094-4087. DOI: `10.1364/OE.`
            `455668`. (Visited on 03/16/2023).

[Reh+23]   Jean Rehbinder et al. "Liquid-Crystal Based Drift-Free Polarization Modulators: Part II. Ultra-stable Stokes and Mueller Polarimeters". In: *Optics Express* 31.6 (Mar. 2023), pp. 10882–10893. ISSN: 1094-4087. DOI: 10.1364/OE.480774. (Visited on 03/10/2023).

[Sca+05]   Valerio Scarani et al. "Quantum Cloning". In: *Reviews of Modern Physics* 77.4 (Nov. 2005), pp. 1225–1256. ISSN: 0034-6861, 1539-0756. DOI: 10.1103/RevModPhys.77.1225. (Visited on 01/12/2023).

[Sca+09]   Valerio Scarani et al. "The Security of Practical Quantum Key Distribution". In: *Reviews of Modern Physics* 81.3 (Sept. 2009), pp. 1301–1350. ISSN: 0034-6861, 1539-0756. DOI: 10.1103/RevModPhys.81.1301. (Visited on 01/12/2021).

[Sco+20]   Alan D. Scott et al. "The QEYSSAT Mission: On-Orbit Demonstration of Secure Optical Communications Network Technologies". In: *Environmental Effects on Light Propagation and Adaptive Systems III*. Ed. by Karin Stein and Szymon Gladysz. Online Only, United Kingdom: SPIE, Sept. 2020, p. 13. ISBN: 978-1-5106-3877-8 978-1-5106-3878-5. DOI: 10.1117/12.2574154. (Visited on 12/10/2020).

[Shi+83]   N. Shibata et al. "Fabrication of Polarization-Maintaining and Absorption-Reducing Fibers". In: *Journal of Lightwave Technology* 1.1 (Mar. 1983), pp. 38–43. ISSN: 1558-2213. DOI: 10.1109/JLT.1983.1072098.

[SK81]   J. Sakai and T. Kimura. "Birefringence and Polarization Characteristics of Single-Mode Optical Fibers under Elastic Deformations". In: *IEEE Journal of Quantum Electronics* 17.6 (June 1981), pp. 1041–1051. ISSN: 0018-9197. DOI: 10.1109/JQE.1981.1071213. (Visited on 03/09/2021).

[SM90]   R. Simon and N. Mukunda. "Minimal Three-Component SU(2) Gadget for Polarization Optics". In: *Physics Letters A* 143.4-5 (Jan. 1990), pp. 165–169. ISSN: 03759601. DOI: 10.1016/0375-9601(90)90732-4. (Visited on 01/17/2023).

[ST19]   Bahaa E. A. Saleh and Malvin Carl Teich. *Fundamentals of photonics*. Third. Wiley & Sons, Limited, John, 2019, p. 1520. ISBN: 978-1-119-50687-4.

[THN88]   Makoto Tsubokawa, Tsunehito Higashi, and Yukiyasu Negishi. "Mode Couplings Due to External Forces Distributed along a Polarization-Maintaining Fiber: An Evaluation". In: *Applied Optics* 27.1 (Jan. 1988), p. 166. ISSN: 0003-6935, 1539-4522. DOI: `10.1364/AO.27.000166`. (Visited on 04/07/2022).

[Tho]   Thorlabs. *Vytran Filament Fusion Splicer*. Accessed: 2023-03-28. Thorlabs. URL: `https://www.thorlabs.com/newgrouppage9.cfm?objectgroup_id=9355`.

[Tho05]   Thorlabs. *Polarization-Maintaining Fiber: Panda Style*. Accessed: 2023-03-28. 2005. URL: `https://www.thorlabs.com/thorproduct.cfm?partnumber=PM780-HP`.

[Xu+20]   Feihu Xu et al. "Secure Quantum Key Distribution with Realistic Devices". In: *Reviews of Modern Physics* 92.2 (May 2020), p. 025002. ISSN: 0034-6861, 1539-0756. DOI: `10.1103/RevModPhys.92.025002`. (Visited on 06/24/2022).

[Yan+12] Zhizhong Yan et al. "An Ultra Low Noise Telecom Wavelength Free Running Single Photon Detector Using Negative Feedback Avalanche Diode". In: *Review of Scientific Instruments* 83.7 (July 2012), p. 073105. ISSN: 0034-6748. DOI: `10.1063/1.4732813`. (Visited on 01/29/2023).

[Zhu94]   Xiaonong Zhu. "Explicit Jones Transformation Matrix for a Tilted Birefringent Plate with Its Optic Axis Parallel to the Plate Surface". In: *Applied Optics* 33.16 (June 1994), p. 3502. ISSN: 0003-6935, 1539-4522. DOI: `10.1364/AO.33.003502`. (Visited on 08/05/2022).

Appendix A

Wave packet model code

Mathematica code used for the wave packet model, attached in pages below.

Defining a wave packet

Wave packet defined in time unit femtoseconds and length unit millimeters.

```
In[ ]:=  R0[t_, T_] := UnitBox[1/T t - 1/2]  (* t is the time variable, T is the time duration *)

A0[t_, T_] := R0[t, T] Sin[ω t]
(* unnormalized rectangular pulse R0 modulated by sinusoid *)
(*R[t_,T_]:= A0[t,T]/(T/2 - Sin[2 T ω]/(4 ω))^(1/2)   (* normalized rectangular pulse *)*)

G0[t_, T_] := 1/(σ Sqrt[2 π]) Exp[-1/2 (t - T/2)^2/σ^2] /. {σ → T/(2 Sqrt[2 Log[2]])}

(* normalized Gaussian envelope *)
R[t_, T_] := G0[t, T] Sin[ω t]
   (* Gaussian wavepacket with underlying oscillations, named R for quick testing *)
```

Defining the PM fiber operations

Each pulse is a list of list of lists. The innermost list represents a single rectangular pulse with its amplitude, pulse shape / time duration, time delay, and phase delay (in that order). The phase delay is unused but left to allow for future changes.

The outermost list has length two (for mode 1 and mode 2), the next list contains every constituent rectangular pulse, the inner most list specifies each rectangular pulse .

```
In[ ]:=  makeH[T_] := {{{1, R[t, T], 0, 0}}, {{0, 0, 0, 0}}};
makeV[T_] := {{{0, 0, 0, 0}}, {{1, R[t, T], 0, 0}}};
makeD[T_] := {{{(1/2)^(1/2), R[t, T], 0, 0}}, {{(1/2)^(1/2), R[t, T], 0, 0}}};
makeA[T_] := {{{(1/2)^(1/2), R[t, T], 0, 0}}, {{-(1/2)^(1/2), R[t, T], 0, 0}}};
getE[state_] := Module[{E1 = 0, E2 = 0},
                   Do[E1 += state[[1]][[i]][[1]] × state[[1]][[i]][[2]] /. t → t - state[[1]][[i]][[3]],
                       {i, 1, Length[state[[1]]]}];
                   Do[E2 += state[[2]][[i]][[1]] × state[[2]][[i]][[2]] /. t → t - state[[2]][[i]][[3]],
                       {i, 1, Length[state[[2]]]}];
                   {E1, E2}
                   ] (* get E-field expression of wave packet *)
getNorm[E_, a_, b_] := Integrate[E[[1]]^2, {t, a, b}] + Integrate[E[[2]]^2, {t, a, b}]
SetAttributes[delayBasis, HoldFirst]

delayBasis[mode_, L_] := Do[mode[[i]][[3]] += B/c L /. {B → 35/10 × 10^-4, c → (3 × 10^8 × 10^3)/10^15},
                   {i, 1, Length[mode]}] (* different group delay of fiber *)

rotateSet[mode1_, mode2_, θ_] := Module[
```

Figure A.1: Defining functions

```
{a = mode1, b = mode2, c = mode1, d = mode2}, (* θ is misalignment in physical space *)
                         Do[a[[i]][[1]] = Cos[θ π/180] mode1[[i]][[1]], {i, 1, Length[mode1]}];
                         Do[b[[i]][[1]] = Sin[θ π/180] mode2[[i]][[1]], {i, 1, Length[mode2]}];
                         Do[c[[i]][[1]] = -Sin[θ π/180] mode1[[i]][[1]], {i, 1, Length[mode1]}];
                         Do[d[[i]][[1]] = Cos[θ π/180] mode2[[i]][[1]], {i, 1, Length[mode2]}];
                         Do[AppendTo[a, b[[j]]], {j, 1, Length[mode2]}];
                         Do[AppendTo[d, c[[j]]], {j, 1, Length[mode1]}];
                         Return[{a, d}]
                      ]
fiberOut[T_, L1_, θ1_] := Module[{mode1 = makeD[T][[1]], mode2 = makeD[T][[2]]},
                         {mode1, mode2} = rotateSet[mode1, mode2, θ1];
                         delayBasis[mode1, L1];
                         {mode1, mode2} = rotateSet[mode1, mode2, -θ1];
                         {mode1, mode2}
                      ] (* output from one PM fiber *)
twoFiberOut[T_, L1_, L2_, θ1_, θ2_] := Module[{mode1 = makeD[T][[1]], mode2 = makeD[T][[2]]},

  {mode1, mode2} = rotateSet[mode1, mode2, θ1]; (* go to axes of first fiber *)
                         delayBasis[mode1, L1]; (* time delay of first fiber *)

  {mode1, mode2} = rotateSet[mode1, mode2, θ2 - θ1]; (* go to axes of second fiber *)
                         delayBasis[mode2, L2]; (* time delay of second fiber *)

  {mode1, mode2} = rotateSet[mode1, mode2, -θ2]; (* go back to lab frame basis *)
                         {mode1, mode2}
                      ] (* output from two PM fibers *)
```

Visibility calculation

The function poco (polarization control) applies the smallest ϕ adjustment needed to bring the two modes in phase . It is done by adjusting the length mismatch to the nearest multiple of oscillation periods. The function visOne computes the visibility dropoff from one fiber alone.

Figure A.2: Defining functions (continued)

```
In[*]:=  poco[state_, LMismatch_, ωState_] :=
         Module[{m1 = state[[1]], δφ = Mod[ B LMismatch / c , 2 π / ωState ] /. {B → 35/10 × 10^-4, c → 3 × 10^8 × 10^3 / 10^15}},

           Do[m1[[i]][[3]] += MinimalBy[{-δφ, 2 π / ωState - δφ}, Abs][[1]], {i, 1, Length[m1]}];
           {m1, state[[2]]}
         ] (* "polarization control" function *)

       visOne[ω0_, T0_, LMismatch_, θ1_] :=
         Module[{EPoco = getE[poco[fiberOut[T0, LMismatch, θ1], LMismatch, ω0]], ID = 0, IA = 0},
           ID =
           NIntegrate[( (EPoco[[1]] + EPoco[[2]]) / √2 )^2, {t, -1, 25}, MinRecursion → 6, PrecisionGoal → 6];
           IA =
           NIntegrate[( (EPoco[[1]] - EPoco[[2]]) / √2 )^2, {t, -1, 25}, MinRecursion → 6, PrecisionGoal → 6];
           ID - IA / ID + IA
         ]
       (* visibility after one fiber, no DGD compensation *)
       vis[ω0_, T0_, L1_, L2_, θ1_, θ2_] :=
         Module[{EPoco = getE[poco[twoFiberOut[T0, L1, L2, θ1, θ2], L1 - L2, ω0]], ID = 0, IA = 0},

           ID = NIntegrate[( (EPoco[[1]] + EPoco[[2]]) / √2 )^2, {t, -3, T0 + 1.2 Max[L1, L2] + 5},

             Method → {"GlobalAdaptive", "MaxErrorIncreases" → 10000},
             WorkingPrecision → 150, MinRecursion → 6, PrecisionGoal → 8];

           IA = NIntegrate[( (EPoco[[1]] - EPoco[[2]]) / √2 )^2, {t, -3, T0 + 1.2 Max[L1, L2] + 5},

             Method → {"GlobalAdaptive", "MaxErrorIncreases" → 10000},
             WorkingPrecision → 150, MinRecursion → 6, PrecisionGoal → 8];
           Abs[ ID - IA / ID + IA ]
         ] (* visibility after two fibers *)
```
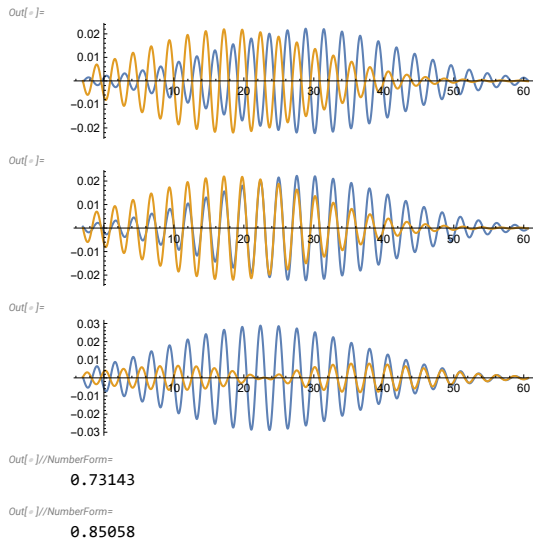
Figure A.3: Visibility calculation

86

Plots for visualization

Plotting the output from a fiber. Using a 30fs pulse for visualization.

```
{ω, T0, L1, L2, θ1, θ2} = {10 π/13, 30, 13, 3, -2, 2};

ETest = getE[twoFiberOut[T0, L1, L2, θ1, θ2]];
EPoco = getE[poco[twoFiberOut[T0, L1, L2, θ1, θ2], L1 - L2, ω]];
Plot[{ETest[[1]], ETest[[2]]}, {t, -3, T0 + 1.2 Max[L1, L2] + 15}, PlotRange → All,
 Exclusions → None, AspectRatio → 1 / 4] (* output without polarization control *)
Plot[{EPoco[[1]], EPoco[[2]]}, {t, -3, T0 + 1.2 Max[L1, L2] + 15}, PlotRange → All,
 Exclusions → None, AspectRatio → 1 / 4] (* output with polarization control *)
Plot[{ EPoco[[1]] + EPoco[[2]]/√2 , EPoco[[1]] - EPoco[[2]]/√2 },

 {t, -3, T0 + 1.2 Max[L1, L2] + 15}, PlotRange → All, Exclusions → None, AspectRatio → 1 / 4]

(* D and A pulses *)
NumberForm[visOne[ω, T0, L1, θ1], 5] (* uncorrected *)
NumberForm[vis[ω, T0, L1, L2, θ1, θ2], 5] (* corrected *)
Clear[ω, T0, L1, L2, θ1, θ2]
```


Out[ ]//NumberForm=
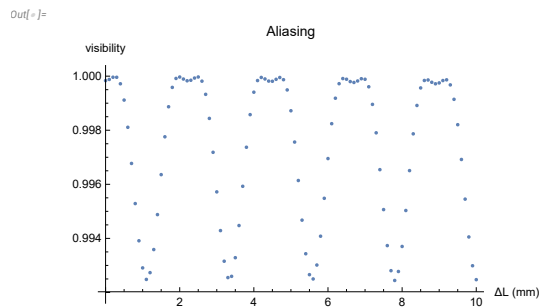0.73143

Out[ ]//NumberForm=
0.85058

The first computation visOne calculates the visibility after a single fiber segment, with no differential group delay correction. The second computation vis calculates the visibility after a second compensating fiber segment.

Figure A.4: Plots show pulse durations far shorter than the timescales of interest in the simulation, for illustrative purposes only, to show the underlying oscillation.

Plot for 1ps wave packet

Code used to generate plot for a 1ps Gaussian wave packet passing through two fibers of a 10mm length mismatch, computed in 0.1mm increments, $\delta\theta1 = +2°$ and $\delta\theta2 = -2°$.

```
{ω, T0, L1, θ1, θ2, maxShift} = { 10 π / 13 , 1000, 60, 2, -2, 6 π};

lenMismatch1ps = Table[{δL, vis[ω, T0, L1, L1 + δL, θ1, θ2]}, {δL, 0, 10, 1 / 10}];
```

In[ ]:=
```
ListPlot[lenMismatch1ps,
        PlotLabel → "Aliasing",
        AxesLabel → {"ΔL (mm)", "visibility"},
        GridLines → {None, {0.99, 0.98}},
        GridLinesStyle → Directive[Thick, Red, Dashed]]
```

Out[ ]=

Figure A.5: Generating data